Observation of Solitons in a Pulsed Magnetron Sputtering Discharge

by

Kristinn B. Gylfason

A thesis submitted in partial satisfaction of the
requirements for the degree of
Master of Science in Electrical Engineering at the University of Iceland

Abstract

Magnetron sputtering devices are used in the deposition of thin films in various sectors of modern industry. Many refinements of the simple dc magnetron have been proposed. The unipolar pulsed magnetron sputtering device is one example. It shows great promise for applications were a high degree of ionization of sputtered particles is necessary. Ion-acoustic solitons are solitary ion density waves that can be modeled by the Korteweg-de Vries equation. Time resolved Langmuir probe measurements in a unipolar pulsed magnetron device indicate the existence of spherical expanding ion-acoustic solitons traveling away from the magnetron target.

Útdráttur

Segulspætur eru notaðar til þess að framleiða þunnar húðir með jónakvörnun. Þær koma víða við sögu í iðnaði samtímans. Kynntar hafa verið ýmsar endurbætur á einföldu jafnstraumssegulspætunni. Einpóla púlsuð segulspæta er dæmi um slíka hönnunartillögu og lofar hún góðu fyrir vinnslu sem krefst mikillar jónunar kvarnaðra agna. Jónaþéttleikabylgjum í rafgasi má lýsa með Korteweg-de Vries jöfnunni. Hún hefur einfaralausnir. Tímaháðar mælingar með Langmuir nema í einpóla púlsaðri segulspætu gefa til kynna að sundurleitnir kúlusamhverfir einfarar ferðist frá skotmarki segulspætunnar.

Contents

List of Figures

Chapter 1

Introduction

The technique of thin film deposition has wide ranging applications in various sectors of modern industry [Proud, 1991]. Thin films are deposited onto bulk material to achieve properties unattainable in the bulk alone. Examples include hard, wear-resistant coatings, low friction coatings, corrosion resistant coatings, decorative coatings and coatings with specific optical, or electrical properties. Additional functionality can be attained by depositing multiple layers of different materials, e.g., optical interference filters that consist of tens or even hundreds of layers alternating between high and low indexes of refraction. When multiple layering is combined with lithographic patterning, micro structures of great variety can be constructed. This is the basic technology of the integrated circuit and micro mechanical device industries [Smith, 1995, p. 1 – 3]. A plethora of thin film deposition methods has been developed but in this work we shall focus on the approach known as *sputtering*.

Sputtering falls in the class of physical vapor deposition (PVD) meth-

ods. The defining characteristic of PVD methods is that the source of the film-forming material is in solid form. The objective of the deposition process is to vaporize the solid source material and transport it to the surface being coated (the substrate) in a controlled manner. In sputtering, this is accomplished by bombarding the source (referred to as the target) with ions that knock out individual atoms or molecules in collisions with the target surface. The ions are supplied by immersing the target in a plasma, obtained by ionizing a gas (often argon) at low pressure. In many cases the neutral sputtered particles gain enough momentum in the collision to shoot across to the substrate and deposit on it [Lieberman and Lichtenberg, 1994, p. 522]. In some cases it is advantageous to ionize the sputtered particles for additional control of the transport. The deposition rate depends on the gas pressure since collisions of sputtered particles with the background gas tend to scatter them off course. This scattering can also negatively effect the coating quality since it enhances the oblique component in the deposition flux [Thornton, 1986]. Therefore it is preferable to operate a sputtering device at low gas pressure.

The popularity of sputtering for thin film deposition can be attributed to the following unique combination of advantages over other techniques: any material can be volatilized by sputtering, compounds are volatilized stoichiometrically, and the film deposition rate can be made uniform over very large areas. Furthermore, the kinetic-energy distribution of sputtered atoms falls largely within the energy window for displacing surface atoms on the depositing film without causing subsurface damage [Smith, 1995, p. 431 – 432].
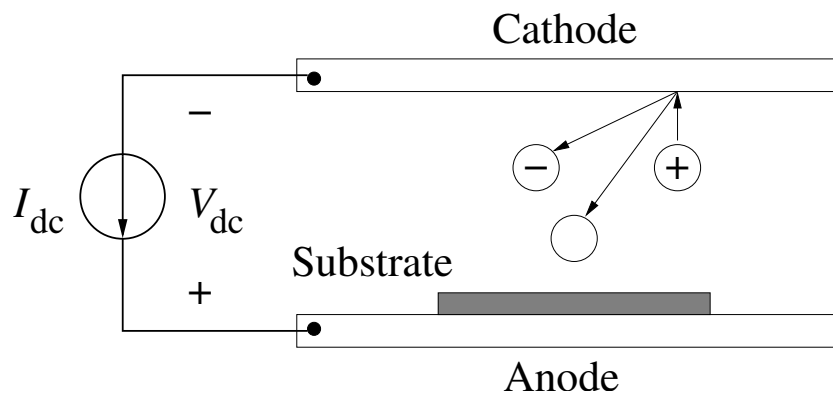
Figure 1.1: A dc glow discharge sputtering device. The upper electrode is the cathode, which serves as a target for ion impact sputtering. The substrate to be coated is placed on the anode. When the positive ions bombard the negative cathode, sputtered neutral particles and energetic secondary electrons are emitted back into the plasma.

1.1   Magnetron sputtering devices

In its simplest form a sputtering device consists of two parallel plates, the cathode and the anode, in a vacuum chamber with a controllable gas pressure. A negative dc voltage in the range $1 - 5$ kV is applied to the cathode and the anode is grounded. The cathode then becomes the source of the film-forming material (the target) and the substrate to be coated is placed on the anode (figure 1.1). The plasma in the chamber is maintained by secondary electrons emitted from the target due to the impact of energetic ions. These electrons are accelerated back into the plasma and, if the operating pressure is high enough, undergo ionizing collisions with the background gas before being lost to the grounded surface. To maintain the discharge the pressure must be kept above 30 mTorr, which is higher than desired for optimum deposition, due to scattering of sputtered particles
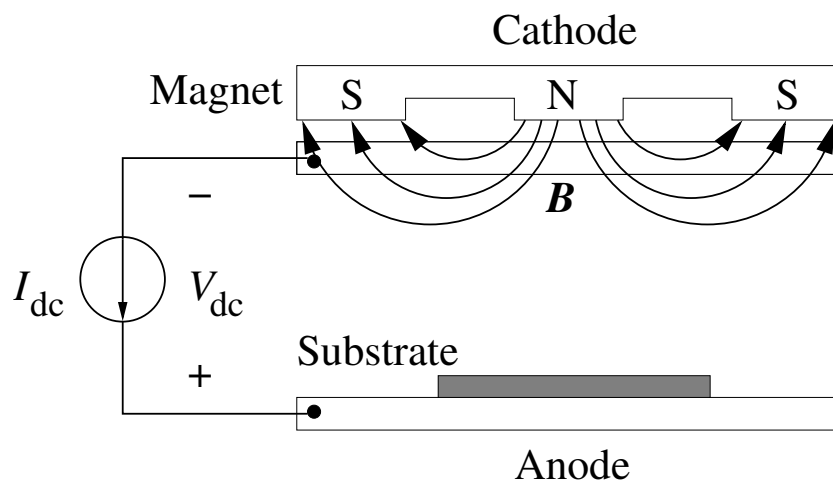
Figure 1.2: A magnetron sputtering device. A magnet is placed at the back of the cathode target with pole pieces at the center and the perimeter. The magnetic field B confines the energetic electrons near the cathode.

by the background gas. This simple configuration, termed *glow discharge sputtering*, yields deposition rates of ≈ 350 Å/min, at best [Lieberman and Lichtenberg, 1994, p. $465 - 466$]. In order to achieve higher rates several enhancements can be made.

One particularly successful enhancement is to confine the secondary electrons in a magnetic trap above the cathode. Such a setup is referred to as a planar *magnetron sputtering device* [Chapin, 1974; Waits, 1978]. The magnetic field is supplied by an axisymetric permanent magnet placed at the back of the cathode plate as shown in figure 1.2. Due to the increased electron confinement the magnetron can operate at voltages as low as 200 V and argon pressures in the $2 - 5$ mTorr range. The magnetic trap enhances the sputtering and the lower operating pressure reduces scattering of sputtered particles by the background gas. The resulting deposition rate is significantly increased to typical values of ≈ 2000 Å/min [Lieber-

man and Lichtenberg, 1994, p. 466 – 467].

Although a general improvement from the simple glow discharge, conventional dc magnetron sputtering processes suffer from a few fundamental problems. These include low target utilization, target poisoning during reactive sputtering, and poor deposition rates for dielectric materials [Kelly and Arnell, 2000]. Increased deposition rates require increased target voltage to achieve a higher plasma density. This leads to a higher ion flux which in turn increases the target thermal load since most of the energy of the positive ions, bombarding the target, is transformed into heat. Several new sputtering systems have been designed to overcome these obstacles. Some of the problems have been alleviated by *pulsing* the applied voltage, others have been solved by additional ionization using an rf induction coil [Rossnagel and Hopwood, 1993, 1994] or additional microwave power [Yonesu et al., 1999]. Refinements of the magnet trap have also been suggested. These include increased magnetic confinement [Kadlec et al., 1990] and an unbalanced magnetron, where the outer ring magnets are strengthened or weakened in an attempt to increase the ion current density in the vicinity of the substrate [Window and Savvides, 1986a,b].

Two principal methods of pulsing have been proposed: *asymmetric bipolar pulsing* and *unipolar pulsing*. Asymmetric bipolar pulsing in the medium frequency range (10 – 250 kHz), has become established as one of the main techniques for deposition of oxide and nitride films [Schiller et al., 1993; Kelly et al., 2000]. Unipolar pulsing utilizes a power supply operating at low (or zero) power level most of the time but pulsing to a

significantly higher level for a short period (e.g., $50 - 100$ μs) each cycle (of length, e.g., 20ms) [Kouznetsov et al., 1999]. This way a substantial increase in the instantaneous plasma density is achieved without increasing the thermal load of the target. Considerable research has been done on this system in recent years. Langmuir probes have been used to record the temporal behavior of the plasma parameters in the substrate vicinity and very high electron densities ($n_\mathrm{e} \approx 6 \times 10^{18}$ m^{-3}) have been obtained [Gudmundsson et al., 2001, 2002]. Furthermore, evidence of improved target utilization has been presented [Kouznetsov et al., 1999] and ionization fractions of sputtered species of 40% for a Ti$_{0.5}$Al$_{0.5}$ target [Macák et al., 2000], 60% for a Ta target [Helmersson et al., 2000], 30% for a Cr target [Ehiasarian et al., 2002] and 90% for a Ti target [Bohlmark et al., 2003] have been reported. This high degree of ionization of sputtered particles opens up possibilities of trench filling applications in integrated circuit production [Rossnagel and Hopwood, 1993] and increased use of ion-surface interaction in designing new thin films [Wei et al., 2000]. Optical emission spectroscopy has also been applied to investigate the time variations of ion and neutral emissions in the target vicinity [Ehiasarian et al., 2002].

Although promising results have been obtained using unipolar pulsed magnetron devices, the dynamics of ion transport in the system have yet to be explained. Insight can be gained from nonlinear fluid theory (section 2.2) and the concepts of solitary waves and solitons.

Figure 1.3: A solitary wave in an aqueduct of the Union Canal created on the occasion of a Conference on Nonlinear Coherent Structures in Physics and Biology in 1995. (Photo by K. Paterson).

1.2 Solitary waves and solitons

The first documented observation of a solitary wave was made by a Scottish engineer, John Scott Russell, in August 1834, when he saw "…a large solitary elevation, a rounded, smooth and well-defined heap of water …" detach itself from the prow of a barge brought to rest and proceed "…without change of form or diminution of speed …" for over two miles along the Union Canal linking Edinburgh with Glasgow. These initial observations were followed by extensive wave-tank experiments on the phenomenon. [Remoissenet, 1996, p. 3].

At the time of their publication, the observations of Russell appeared to contradict the nonlinear shallow-water wave theory of Airy (1845), which predicts that a wave with elevation of finite amplitude cannot propagate without change of form: it steepens and eventually breaks. On the other
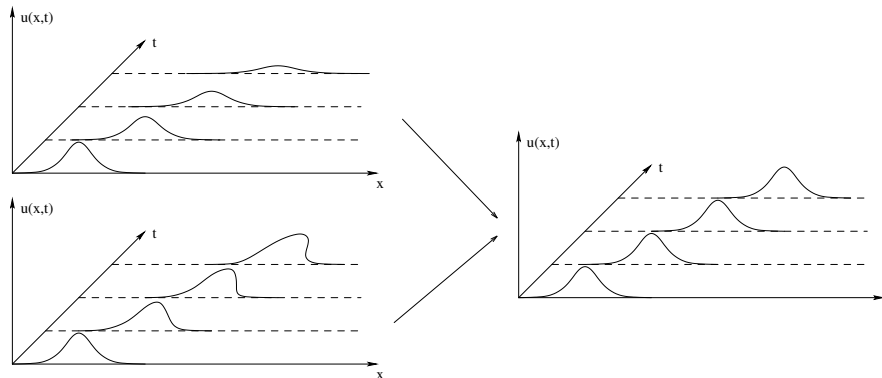
Figure 1.4: The formation of a solitary wave (right) is the result of a balance between the effects of dispersion (top left) and nonlinearity (bottom left).

hand, Stokes (1874) showed that waves of finite amplitude and permanent form are possible in deep water, but they are periodic.

The controversy over Russell's observations arises because the non-linear shallow-water theory neglects dispersion, which generally tends to prevent wave steepening. It was resolved by Joseph Boussinesq (1871) and independently by Lord Rayleigh (1876), who showed that, if one ignores dissipation, *the steepening of the wave can be balanced by the dispersion, leading to a wave of permanent form.* This effect is shown schematically in figure 1.4 and elaborated on in section 2.1.

In 1895 Korteweg and de Vries derived a model equation (incorporating the effects of surface tension) which describes the unidirectional propagation of long waves in water of relatively shallow depth. This equation has become much celebrated and is now known as the Korteweg-de Vries equation or KdV for short:

$$\frac{\partial u}{\partial t} + \alpha u \frac{\partial u}{\partial x} + \beta \frac{\partial^3 u}{\partial x^3} = 0, \qquad \alpha, \beta \quad \text{constants.} \tag{1.1}$$

Korteweg and de Vries showed that periodic solutions, which they named cnoidal waves, could be found in closed form and without further approximations [Remoissenet, 1996, p. 5 – 6]. Moreover, they found a localized solution

$$u(x,t) = \frac{3v}{\alpha}\text{sech}^2 \left[\frac{1}{2}\sqrt{\frac{v}{\beta}}(x - vt) \right],$$ (1.2)

which represents a single hump of elevation $3v/\alpha$, traveling with velocity v. This hump is the solitary wave discovered experimentally by Scott Russell.

For a long time, the solitary wave was considered a rather unimportant curiosity in the mathematical structure of nonlinear wave theory. It was however brought into the mainstream of research by Fermi, Pasta, and Ulam [1955]. They were exploring heat-transfer in crystal lattices with nonlinear interactions, by computer simulations and found, much to their surprise, that the system showed very little tendency toward equipartition of energy among the degrees of freedom. They applied a large amplitude sinusoidal signal as an initial condition. Due to the nonlinearity of the structure, it was expected that harmonics would develop and all of the energy would be randomly thermalized as time progressed. This thermalization was found in their calculation for the first time steps but at a certain time most of the energy "recurred" to the fundamental mode and the original sinusoidal signal reappeared. This process then repeated itself [Lonngren, 1983].

The unexpected results of Fermi, Pasta and Ulam motivated Zabuski and Kruskal [1965] to re-investigate the problem. By a continuum ap-

proximation this led them to study the KdV equation. From numerical simulations they found that robust pulse-like waves can propagate in a system modeled by such an equation. Zabusky and Kruskal coined the word *soliton* to describe these particle-like solitary waves, which can collide with each other and preserve their identities after the collision. In most of the physics literature the terms solitary wave and soliton are used interchangeably but in this work we shall confine ourselves to the latter one.

Gardner et al. [1967] made an important contribution to the development of the theory. They showed that, if the initial shape of the wave is sufficiently localized the analytical solution of the KdV equation can be obtained. Their solution shows that, given sufficiently long time, the initial pulse evolves into one or more solitons and a dispersive small-amplitude tail. The total number of solitons depends on the initial shape. These theoretical results were in remarkable agreement with many of the experimental results obtained by John Scott Russell more than one hundred and fifty years earlier [Remoissenet, 1996, p. 7 – 8].

1.3 Ion-acoustic solitons in plasma

In 1966 Washimi and Taniuti [1966] showed that a collision-less plasma of cold ions and warm electrons can be modeled by the KdV equation. They started out with a simplified subset of the plasma fluid equations (section

2.2) expressed in normalized quantities (section 2.3):

$$\frac{\partial n_i'}{\partial t'} + \frac{\partial}{\partial x'}(n_i' u_i') = 0 \tag{1.3}$$

$$\frac{\partial u_i'}{\partial t'} + u_i'\frac{\partial u_i'}{\partial x'} = E' \tag{1.4}$$

$$\frac{\partial n_e'}{\partial x'} = -n_e' E' \tag{1.5}$$

$$\frac{\partial E'}{\partial x'} = n_i' - n_e' \tag{1.6}$$

in which n_i' and n_e' denote the densities of ions and electrons, respectively, u_i' is the flow velocity of ions, E' is the electric field, x' is the space coordinate and t' the time variable. By mathematical manipulations (section 2.3) they showed that the system (1.3)–(1.6) can be simplified to the KdV equation

$$\frac{\partial n_1}{\partial \eta} + n_1\frac{\partial n_1}{\partial \xi} + \frac{1}{2}\frac{\partial^3 n_1}{\partial \xi^3} = 0, \tag{1.7}$$

where n_1 is a first order perturbation of the ion density n_i' and η and ξ are scaled time and space variables, respectively. This result was a prediction of the existence of *ion-acoustic solitons*.

Ion-acoustic solitons were first observed experimentally in a double-plasma device (chapter 3) by Ikezi et al. [1970]. Since the initial observation, they have been the subject of numerous experiments. These include: multiple soliton production in a double-plasma device [Hershkowitz et al., 1972; Ikezi, 1973]; excitation of cylindrical [Hershkowitz and Romesser, 1974] and spherical [Ze et al., 1979a] ion-acoustic solitons; wide soliton generation in an ion-beam-plasma system [Lee et al., 1996]; and ion-acoustic

shock formation in a Q-machine with negative ions [Takeuchi et al., 1998] and in a dusty double-plasma device [Nakamura et al., 1999].

Recently, a report on the temporal behavior of the electron density in a unipolar high-power pulsed magnetron sputtering device, with a tantalum target, showed some interesting features [Gudmundsson et al., 2002]. In figure 1.5 we reprint two of their graphs showing the electron density in the device as a function of time from pulse initiation. Figure 1.5 (a) shows the effect of background pressure, in the range 5 – 20 mTorr, on the electron density at 9 cm below the target. In general the plot shows an increase in electron density with increased pressure. Looking more closely at the time evolution, considerable structure is seen in the signal. The first 400 μs are dominated by rapid fluctuations at all pressures. Beyond the initial fluctuations, a hump at approximately 600 μs, growing with increasing pressure, is noticed. This phenomenon remains unexplained. Figure 1.5 (b) shows the initial electron peaks at 2 mTorr in more detail and follows their evolution from 9 to 17 cm below the target. They noticed that these peaks are traveling away from the target at a fixed velocity. This observation of electron density waves triggered the work described here. Our aim is to show that these waves are in fact ion-acoustic solitons of the type modeled by Washimi and Taniuti.

10^{20}

10^{19}

$n_{\mathrm{e}}\ [\mathrm{m}^{-3}]$

10^{18}

10^{17}

10^{16}

(a)

5 mTorr

10 mTorr

20 mTorr

100

300

500

0   200   400   600   800   1000

$t\ [\mu s]$

10^{19}

10^{20}

$n_{\mathrm{e}}\ [\mathrm{m}^{-3}]$

10^{18}

10^{17}

(b)

9 cm

13 cm

17 cm

600

800

1000

(a)

0   100   200   300   400   500

$t\ [\mu s]$
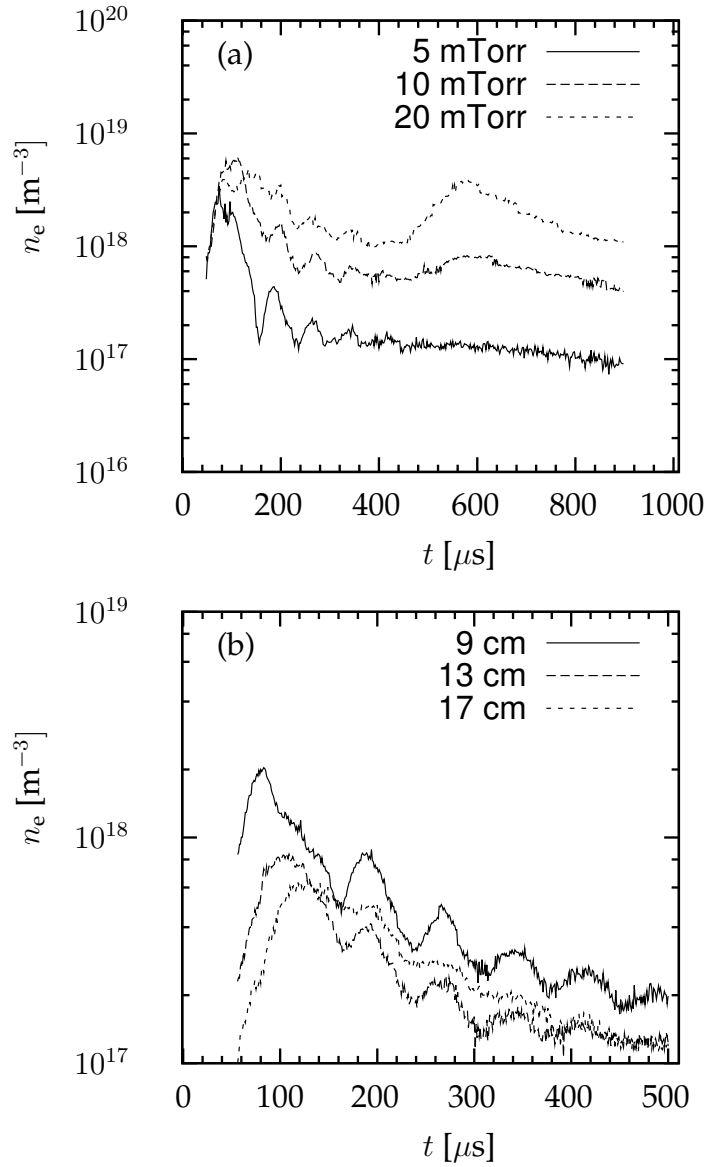
Figure 1.5: Electron density n_{e} as a function of time t from pulse initiation: (a) at 9 cm below the target for gas pressure of 5, 10 and 20 mTorr and (b) at a pressure of 2 mTorr for the first 500 μs at 9, 13 and 17 cm below the target. The magnetron was operated with a tantalum target. The voltage pulse length was 100 μs and the average power 300 W [Gudmundsson et al., 2002].

Chapter 2

Waves in plasma

Most of the engineering feats of the twentieth century were accomplished using linear models of the physical world. In some cases, e.g., electromagnetism, the linear models are highly successful in predicting observed behavior, but in others we are faced with phenomena that are inherently nonlinear and can therefore not be grasped with the help of a linear model. In this chapter we shall give a compact overview of such a phenomenon: ion-acoustic solitons in plasma. First a brief discussion is given on waves in nonlinear dispersive systems. This is followed by a review of how a plasma can be modeled as a fluid. Finally we show how the Korteweg-de Vries equation is used to describe one-dimensional finite amplitude ion waves in a plasma.

2.1 A brief review of waves

The soliton concept depends on familiarity with the effects of dispersion and nonlinearity and thus a brief review of waves, in systems dominated by these properties, is in order. By referring to examples from transmission line theory, we will present a mostly qualitative discussion.

2.1.1 Linear systems without dispersion
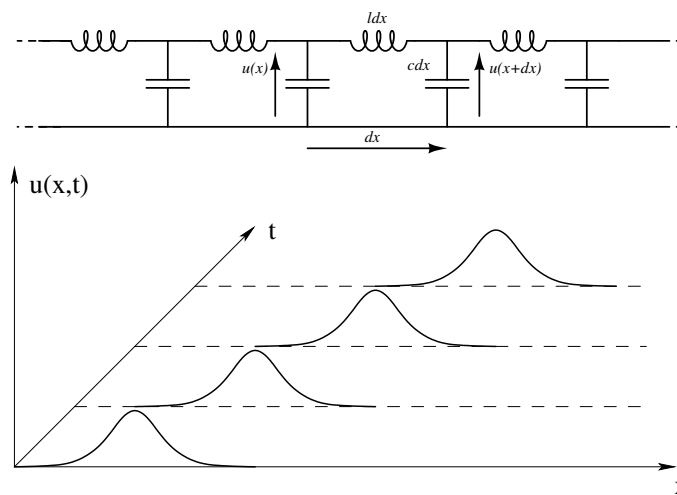
Figure 2.1: A linear transmission line with distributed inductance l and capacitance c, per unit length (top), and a general pulse traversing the line (bottom).

As our first example consider a general pulse traversing a linear transmission line modeled by a distributed inductance l and a distributed capacitance c, a simple linear system without dispersion. By applying Kirchhoff's voltage law to the model in figure 2.1 we find that the voltage wave

$u(x, t)$ traversing the line must satisfy the wave equation

$$\frac{\partial^2 u}{\partial t^2} - v_0^2 \frac{\partial^2 u}{\partial x^2} = 0, \qquad v_0 = \frac{1}{\sqrt{lc}}. \tag{2.1}$$

Assume solutions of the form

$$u(x, t) = u_0 \cos k(x - v_0 t) = u_0 \cos(kx - \omega t) \tag{2.2}$$

and we get the dispersion relation

$$\omega = v_0 k, \tag{2.3}$$

i.e. different frequency components of the pulse travel with the same speed and the pulse retains its form (figure 2.1) [Remoissenet, 1996, p. 12 – 15].

2.1.2 Linear dispersive systems

We now add dispersion to our transmission line model by taking induction between conductors into account (figure 2.2). The wave equation for a linear transmission line with parallel induction is

$$\frac{\partial^2 u}{\partial t^2} - v_0^2 \frac{\partial^2 u}{\partial x^2} + \omega_0^2 u = 0, \qquad \omega_0^2 = \frac{1}{l_2 c}. \tag{2.4}$$

Again we assume solutions of the form

$$u(x, t) = u_0 \cos(kx - \omega t) \tag{2.5}$$
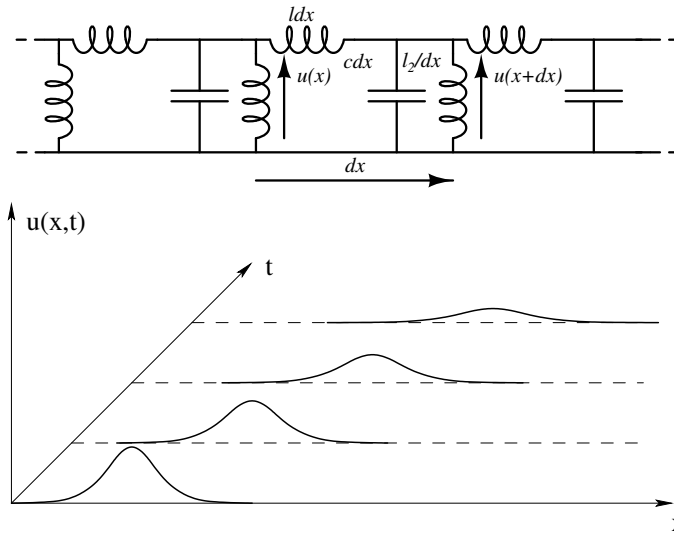
Figure 2.2: A linear dispersive transmission line with distributed inductance l and capacitance c, in parallel with an inductance l_2, per unit length (top), and a general pulse traversing the line (bottom).

and get the dispersion relation

$$\omega = \sqrt{\omega_0^2 + v_0^2 k^2}. \tag{2.6}$$

In contrast to the non-dispersive line, different frequency components travel with different speeds and the pulse in figure 2.2 is dispersed as it moves through the system [Remoissenet, 1996, p. 21 – 23].

2.1.3 Nonlinear systems without dispersion

In comparison with the last case, consider a nonlinear system without dispersion. An example is the transmission line shown in figure 2.3, with a voltage dependent capacitance $c(u) = C_0(1 - 2bu)$ between conductors (C_0
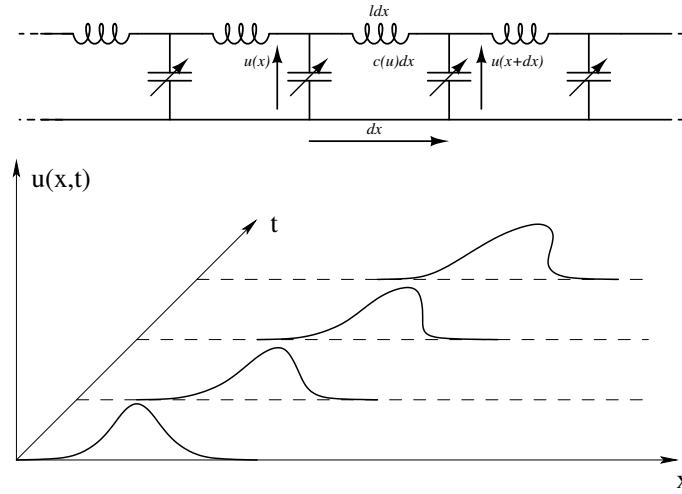
Figure 2.3: A nonlinear non-dispersive transmission line with distributed inductance l and a voltage dependent capacitance $c(u)$ per unit length (top) and a general pulse traversing the line (bottom).

and b constants). It can be described by the equation

$$\frac{\partial^2 u}{\partial t^2} - \frac{1}{lC_0}\frac{\partial^2 u}{\partial x^2} = \frac{\partial^2 u^2}{\partial t^2}.$$

(2.7)

One can show that the solution has the form

$$u(x,t) = f\{x \pm [lc(u)]^{-\frac{1}{2}}t\}$$

(2.8)

and that the velocity of propagation depends on the amplitude

$$v = [lc(u)]^{-\frac{1}{2}} = \frac{1}{\sqrt{lC_0(1-2bu)}},$$

(2.9)

i.e., the top of the pulse in figure 2.3 moves faster than the base resulting in a steepening of the wavefront [Remoissenet, 1996, 37 – 41].

2.1.4 Nonlinear dispersive systems
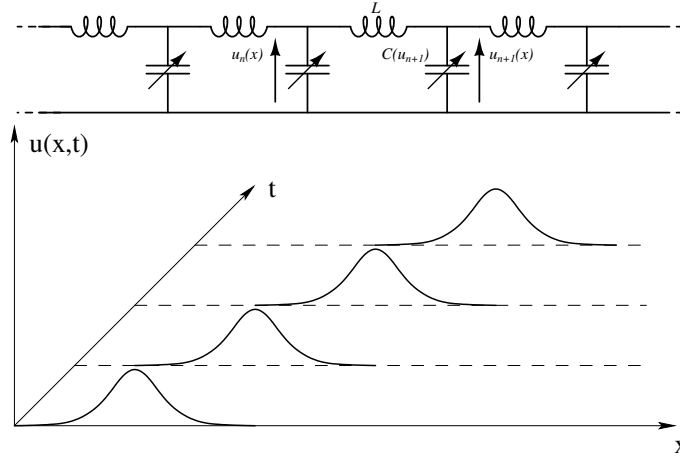
Figure 2.4: A discrete transmission line (network) with an inductance L and a voltage dependent capacitance $C(u)$, per unit section (top), and a general pulse traversing the line (bottom).

Now we consider a system that exhibits both nonlinear and dispersive behavior. An example is a discrete transmission line with a voltage dependent capacitance $C(u) = C_0(1 - 2bu)$ and inductance L in each unit section shown in figure 2.4. It can be described by the equation

$$\frac{\partial^2 u}{\partial t^2} - \left(\frac{\delta^2}{LC_0}\right)\frac{\partial^2 u}{\partial x^2} = \left(\frac{\delta^4}{12LC_0}\right)\frac{\partial^4 u}{\partial x^4} + b\frac{\partial^2 u^2}{\partial t^2}, \tag{2.10}$$

where δ represents a hypothetical unit cell length. The dispersive and nonlinear terms on the right can cancel each other leading to a solution of permanent form

$$u(x,t) = \frac{3}{2b}\frac{v^2 - v_0^2}{v^2}\text{sech}^2\left[\frac{\sqrt{3(v^2 + v_0^2)}}{v_0}\frac{(x - vt)}{\delta}\right], \tag{2.11}$$

where v is the velocity of the soliton and $v_0 = \delta/\sqrt{LC}$.

For waves traveling with a small amplitude in one direction, equation (2.10) simplifies to the Korteweg-de Vries equation

$$\frac{\partial u}{\partial t} + \alpha u \frac{\partial u}{\partial x} + \beta \frac{\partial^3 u}{\partial x^3} = 0, \qquad \alpha, \beta \quad \text{constants,} \qquad (2.12)$$

using a mathematical method termed the *reductive perturbation technique* [Remoissenet, 1996, 41 – 42] (section 2.3).

2.2 Modeling plasma as a fluid

A partially ionized plasma consists of electrons, ions, and neutral atoms and/or molecules. The particles interact through collisions and electromagnetic fields. Their interactions can be studied at the particle level but to the plasma processing experimentalist a useful model is expressed in easily measurable quantities such as fluid velocity and particle density. The rigorous development of the theory from particle level to the *fluid model* of a plasma is the subject of many fine books on plasma physics [Nicholson, 1983; Chen, 1984; Dendy, 1993] but in this section we shall present the results relevant to our subject.

The traditional approach to the development of the fluid model starts with the exact description of the motion of each particle in form of the *Klimontovich equation* [Nicholson, 1983, chapter 3]. If there are N particles in three-dimensional space, and each particle has a position and a velocity, the total number of coordinates is $6N$. A typical plasma density might

be 10^{16} ion-electron pairs per m^3 so the calculations quickly become intractable. The solution is to use an approximate statistical theory formulated in the *Vlasov equation*

$$\frac{\partial f}{\partial t} + \boldsymbol{v} \cdot \frac{\partial f}{\partial \boldsymbol{x}} + \frac{q}{m}(\boldsymbol{E} + \boldsymbol{v} \times \boldsymbol{B}) \cdot \frac{\partial f}{\partial \boldsymbol{v}} = 0, \qquad (2.13)$$

where m is the mass and q is the charge of the species under consideration. $\boldsymbol{E}$ and $\boldsymbol{B}$ are the electric and magnetic fields respectively and $f(\boldsymbol{x}, \boldsymbol{v}, t)$ is a velocity distribution function such that

$$f(\boldsymbol{x}, \boldsymbol{v}, t)\mathrm{d}x\mathrm{d}y\mathrm{d}z\mathrm{d}v_x\mathrm{d}v_y\mathrm{d}v_z \qquad (2.14)$$

is the number of particles in the volume element $\mathrm{d}x\mathrm{d}y\mathrm{d}z$ at the position $\boldsymbol{x}$, and in the element $\mathrm{d}v_x\mathrm{d}v_y\mathrm{d}v_z$ in velocity space with the velocity $\boldsymbol{v}$, at time t [Nicholson, 1983, chapter 6]. The fluid theory is then developed by taking the first few velocity moments of the Vlasov equation [Nicholson, 1983, p. 129] and when combined with Maxwell's equations the fluid equations provide a complete, but approximate, description of plasma physics. The following discussion introduces the fluid equations heuristically and closely follows Chen [1984, chapter 3].

2.2.1 Equation of continuity

In the fluid approximation, we consider the plasma to be composed of two or more inter-penetrating fluids, one for each species of particles. The conservation of matter requires that the total number of particles N in a

volume V can change only if there is a net flux of particles across the surface S bounding that volume. If n is the particle density and $\boldsymbol{u}$ is the fluid velocity then the particle flux density is $n\boldsymbol{u}$. As a result we have, by the divergence theorem,

$$\frac{\partial N}{\partial t} = \int_V \frac{\partial n}{\partial t} \mathrm{d}V = -\oint n\boldsymbol{u} \cdot \mathrm{d}\boldsymbol{S} = -\int_V \boldsymbol{\nabla} \cdot (n\boldsymbol{u})\mathrm{d}V. \qquad (2.15)$$

Since this must hold true for any volume V, the integrands must be equal and thus:

$$\frac{\partial n}{\partial t} + \boldsymbol{\nabla} \cdot (n\boldsymbol{u}) = 0. \qquad (2.16)$$

There is one such equation of continuity for each species. Any sources or sinks of particles are to be added to the right-hand side. The rigorous derivation of the continuity equation is done by taking the zeroth order velocity moment of the Vlasov equation [Elliot, 1993, p. 39].

2.2.2   The fluid equation of motion

Maxwell's equations give us the electric field $\boldsymbol{E}$ and the magnetic field $\boldsymbol{B}$ for a particular state of the plasma. To solve the self-consistent problem, we must also have an equation giving the plasma's response to given $\boldsymbol{E}$ and $\boldsymbol{B}$ fields. In the simplest case, a fully ionized plasma with only one species of ions, we shall need two equations of motion, one for the positive ion fluid and one for the negative electron fluid. A more rigorous description of a partially ionized gas would also include an equation for the fluid of neutral atoms and/or molecules. The neutral fluid interacts with the

ions and electrons only through collisions and will not be considered here since we are only interested in plasma at low pressure. The ion and electron fluids will interact with each other even in the absence of collisions, because of the $\boldsymbol{E}$ and $\boldsymbol{B}$ fields they generate.

Assume first that there are no thermal motions. Newton's second law of motion for the plasma fluid is then

$$mn \left[\frac{\partial \boldsymbol{u}}{\partial t} + (\boldsymbol{u} \cdot \boldsymbol{\nabla})\boldsymbol{u} \right] = qn(\boldsymbol{E} + \boldsymbol{u} \times \boldsymbol{B}). \tag{2.17}$$

In the *convective derivative* on the left, the $\partial \boldsymbol{u}/\partial t$ represents an acceleration due to an explicitly time-varying fluid velocity $\boldsymbol{u}$ and the second "inertial" term $(\boldsymbol{u} \cdot \boldsymbol{\nabla})\boldsymbol{u}$ represents an acceleration even for a steady fluid flow ($\partial \boldsymbol{u}/\partial t = 0$) having a spatially varying $\boldsymbol{u}$ [Lieberman and Lichtenberg, 1994, p. 34].

When thermal motions are taken into account, a pressure force has to be added to the right-hand side of equation (2.17). This force arises from random motion of particles in and out of a fluid element. The fluid equation then becomes

$$mn \left[\frac{\partial \boldsymbol{u}}{\partial t} + (\boldsymbol{u} \cdot \boldsymbol{\nabla})\boldsymbol{u} \right] = qn(\boldsymbol{E} + \boldsymbol{u} \times \boldsymbol{B}) - \boldsymbol{\nabla} p \tag{2.18}$$

where $\boldsymbol{\nabla} p$ is the isotropic pressure gradient force. Rigorously, the fluid equation of motion is derived by taking the first order velocity moment of the Vlasov equation [Elliot, 1993, p. 40]. The equation describes the conservation of momentum.

2.2.3 Equation of state

One more relation is needed to close the system of equations. For this, we can use the thermodynamic equation of state relating p to n:

$$p = Cn^\gamma, \tag{2.19}$$

where C is a constant and γ is the ratio of specific heats C_p/C_v. The term $\boldsymbol{\nabla} p$ is therefore given by

$$\frac{\boldsymbol{\nabla} p}{p} = \gamma \frac{\boldsymbol{\nabla} n}{n}. \tag{2.20}$$

For isothermal compression, we have

$$\boldsymbol{\nabla} p = \boldsymbol{\nabla}(nkT) = kT\boldsymbol{\nabla} n, \tag{2.21}$$

where k is the Boltzmann constant and T is the temperature of the species, so that $\gamma = 1$. The thermodynamic equation of state is rigorously derived by taking the second order velocity moment of the Vlasov equation and describes the conservation of energy [Elliot, 1993, p. 42].

2.2.4 The complete set of fluid equations

For a plasma with only two species, ions and electrons, the charge and current densities are given by

$$\sigma = n_i q_i + n_e q_e, \tag{2.22}$$

$$\boldsymbol{j} = n_i q_i \boldsymbol{u}_i + n_e q_e \boldsymbol{u}_e. \tag{2.23}$$

The complete set of fluid equations is then:

$$\varepsilon_0 \boldsymbol{\nabla} \cdot \boldsymbol{E} = n_i q_i + n_e q_e, \tag{2.24}$$

$$\boldsymbol{\nabla} \times \boldsymbol{E} = -\frac{\partial \boldsymbol{B}}{\partial t}, \tag{2.25}$$

$$\boldsymbol{\nabla} \cdot \boldsymbol{B} = 0, \tag{2.26}$$

$$\mu_0^{-1} \boldsymbol{\nabla} \times \boldsymbol{B} = n_i q_i \boldsymbol{u}_i + n_e q_e \boldsymbol{u}_e + \varepsilon \frac{\partial \boldsymbol{E}}{\partial t}, \tag{2.27}$$

$$\frac{\partial n_j}{\partial t} + \boldsymbol{\nabla} \cdot (n_j \boldsymbol{u}_j) = 0, \quad j = i, e, \tag{2.28}$$

$$m_j n_j \left[\frac{\partial \boldsymbol{u_j}}{\partial t} + (\boldsymbol{u_j} \cdot \boldsymbol{\nabla}) \boldsymbol{u_j} \right] = q_j n_j (\boldsymbol{E} + \boldsymbol{u_j} \times \boldsymbol{B}) - \boldsymbol{\nabla} p_j, \quad j = i, e, \tag{2.29}$$

$$p_j = C_j n_j^{\gamma_j}, \quad j = i, e. \tag{2.30}$$

There are 16 scalar unknowns: n_i, n_e, p_i, p_e, $\boldsymbol{u}_i$, $\boldsymbol{u}_e$, $\boldsymbol{E}$ and $\boldsymbol{B}$. There are apparently 18 scalar equations if we count each vector equation as three scalar equations. However, two of Maxwell's equations are superfluous, since equations (2.24) and (2.26) can be recovered from the divergences of equations (2.27) and (2.25) respectively. The simultaneous solution of this set of 16 equations in 16 unknowns gives a self-consistent set of fields and motions in the fluid approximation.

2.3   The Korteweg-de Vries equation

As introduced earlier, Washimi and Taniuti [1966] showed, by the reductive perturbation technique, that the Korteweg-de Vries equation describes one-dimensional finite amplitude ion waves. They start by making a few simplifying assumptions to reduce the number of fluid equations (2.24) –

(2.30). Their first assumption is to neglect the thermal motion of the ions (cold ions). The fluid equations of ion motion (2.29) and continuity (2.28) in this case are:

$$m_i \left(\frac{\partial u_i}{\partial t} + u_i \frac{\partial u_i}{\partial x} \right) = -e \frac{\partial \Phi}{\partial x} \tag{2.31}$$

and

$$\frac{\partial n_i}{\partial t} + \frac{\partial (n_i u_i)}{\partial x} = 0, \tag{2.32}$$

where the electric field E has been replaced with the negative derivative of the potential $-\partial \Phi / \partial x$. Next they assume isothermal electrons and hence the electron equation of state (2.30) gives

$$p_e = n_e k T_e. \tag{2.33}$$

Finally they ignore the electron mass ($m_e = 0$) and thus the electron equation of motion (2.29) yields

$$e n_e \frac{\partial \Phi}{\partial x} = \frac{\partial n_e}{\partial x}, \tag{2.34}$$

which integrates to give Boltzmann distributed electrons

$$n_e = n_0 \exp \left(\frac{e \Phi}{k T_e} \right), \tag{2.35}$$

where n_0 is the equilibrium background density. The set of equations is closed with Poissions's equation (obtained from 2.24)

$$\frac{\partial^2 \Phi}{\partial x^2} = \frac{e}{\epsilon_0} \left(n_0 \exp \left(\frac{e \Phi}{k T_e} \right) - n_i \right). \tag{2.36}$$

By changing to the following dimensionless variables the clutter of physical constants is removed:

$$x' = \left(\frac{n_0 e^2}{\epsilon_0 k T_e} \right)^{\frac{1}{2}} x = \frac{x}{\lambda_D}, \tag{2.37}$$

$$t' = \left(\frac{n_0 e^2}{\epsilon_0 m_i} \right)^{\frac{1}{2}} t, \tag{2.38}$$

$$\Phi' = \frac{e\Phi}{k T_e}, \tag{2.39}$$

$$n' = \frac{n_i}{n_0}, \tag{2.40}$$

$$u' = \left(\frac{m_i}{k T_e} \right)^{\frac{1}{2}} u_i = \frac{u_i}{c_s}. \tag{2.41}$$

In the new variables the set of equations becomes

$$\frac{\partial u'}{\partial t'} + u' \frac{\partial u'}{\partial x'} = -\frac{\partial \Phi'}{\partial x'}, \tag{2.42}$$

$$\frac{\partial n'}{\partial t'} + \frac{\partial n' u'}{\partial x'} = 0, \tag{2.43}$$

$$\frac{\partial^2 \Phi'}{\partial x'^2} = e^{\Phi'} - n', \tag{2.44}$$

with boundary conditions $n' \to 1$, $u' \to 0$ and $\Phi' \to 0$ as $x' \to \infty$.

To recover the KdV equation, the wave amplitude is expanded in terms of a perturbation parameter δ and one order higher than linear kept. This step restricts the validity of the derivation to small but finite-amplitude

waves. The expansion is:

$$n' = 1 + \delta n_1 + \delta^2 n_2 + \cdots,$$
$$\Phi' = \delta \Phi_1 + \delta^2 \Phi_2 + \cdots, \tag{2.45}$$
$$u' = \delta u_1 + \delta^2 u_2 + \cdots,$$

Since only long waves are of interest, we transform to the scaled variables

$$\xi = \delta^{\frac{1}{2}}(x' - t') \tag{2.46}$$

and

$$\tau = \delta^{\frac{3}{2}} t' \tag{2.47}$$

so that

$$\frac{\partial}{\partial t'} = \delta^{\frac{3}{2}} \frac{\partial}{\partial \tau} - \delta^{\frac{1}{2}} \frac{\partial}{\partial \xi}, \tag{2.48}$$

$$\frac{\partial}{\partial x'} = \delta^{\frac{1}{2}} \frac{\partial}{\partial \xi}. \tag{2.49}$$

By operating with (2.49) on (2.45) and substituting into (2.44), it is found that the lowest-order terms are proportional to δ and these give

$$\Phi_1 = n_1. \tag{2.50}$$

Doing the same in equations (2.42) and (2.43), it is found that the lowest-

order terms are proportional to $\delta^{\frac{3}{2}}$ and these give

$$\frac{\partial u_1}{\partial \xi} = \frac{\partial \Phi_1}{\partial \xi} = \frac{\partial n_1}{\partial \xi}. \tag{2.51}$$

Since all vanish as $\xi \to \infty$, integration gives

$$n_1 = \Phi_1 = u_1 \equiv U. \tag{2.52}$$

Thus the normalization is such that all the linear perturbations are equal and can be called U. Next the terms proportional to δ^2 in equation (2.44) and to $\delta^{5/2}$ in equations (2.42) and (2.43) are collected. This yields the set:

$$\frac{\partial^2 \Phi_1}{\partial \xi^2} = \Phi_2 - n_2 + \frac{1}{2}\Phi_1^2, \tag{2.53}$$

$$\frac{\partial u_1}{\partial \tau} - \frac{\partial u_2}{\partial \xi} + u_1 \frac{\partial u_1}{\partial \xi} = -\frac{\partial \Phi_2}{\partial \xi}, \tag{2.54}$$

$$\frac{\partial n_1}{\partial \tau} - \frac{\partial n_2}{\partial \xi} + \frac{\partial}{\partial \xi}(u_2 + n_1 u_1) = 0. \tag{2.55}$$

Solving for n_2 in (2.53) and for $\partial u_2 / \partial \xi$ in (2.54) and substituting into (2.55) yields:

$$\frac{\partial n_1}{\partial \tau} + \frac{\partial^3 \Phi_1}{\partial \xi^3} - \frac{\partial \Phi_2}{\partial \xi} - \frac{1}{2}\frac{\partial \Phi_1^2}{\partial \xi} + \frac{\partial u_1}{\partial \tau} + u_1 \frac{\partial u_1}{\partial \xi} + \frac{\partial \Phi_2}{\partial \xi} + \frac{\partial}{\partial \xi}(n_1 u_1) = 0. \tag{2.56}$$

Fortunately, Φ_2 cancels out. By replacing all first-order quantities by U the KdV equation is obtained:

$$\frac{\partial U}{\partial \tau} + U\frac{\partial U}{\partial \xi} + \frac{1}{2}\frac{\partial^3 U}{\partial^3 \xi} = 0. \tag{2.57}$$

Thus, ion waves of amplitude one order higher than linear are described by the Korteweg-de Vries equation. In experiments on ion-acoustic solitons the value n_1 is usually measured in terms of the relative density perturbation $(n - n_0)/n_0$, where n is the absolute density of the species and n_0 is the quiescent background density. In the presentation of the derivation we have followed Chen [1984, p. 331 – 336] and Dodd et al. [1982, p. 237 – 242].

Modified KdV equations describing one-dimensional solitons (dependent only on radius r) with cylindrical [Maxon and Viecelli, 1974a] and spherical [Maxon and Viecelli, 1974b] symmetry have also been derived.

2.4 Ion-acoustic soliton characteristics

Hershkowitz and Romesser [1974] summarized the distinguishing characteristics of one-dimensional solitons. These features are common to one-dimensional solitons in planar, cylindrical and spherical geometries and provide a reference for comparison with experimental data:

1. Arbitrary positive (compressive) density perturbations evolve after sufficient time into a superposition of spatially separated solitons.

2. The number and amplitude of the solitons is determined by the solution of a time-independent Schrödinger equation with a potential that is proportional to the initial spatial density perturbation. One soliton is formed for each bound state with soliton amplitude proportional to the energy eigenvalues.

3. In a plasma with background ion density n_0 a soliton with a peak density of n_{peak} will travel with a velocity of

$$u = [1 + 1/3(\delta n/n_0)]c_{\text{s}}, \tag{2.58}$$

where $\delta n = n_{\text{peak}} - n_0$ and $c_s = (e\text{T}_{\text{e}}/m_{\text{i}})^{1/2}$ is the ion acoustic velocity (T_{e} is the electron temperature expressed in the more practical units of eV).

4. The spatial width D of a soliton is proportional to $(\delta n/n_0)^{-1/2}$, which implies

$$D^2\delta n/n_0 = \text{constant.} \tag{2.59}$$

5. Solitons retain their identity upon collision with other solitons.

In addition to characteristic 2 it has been shown that to the continuous spectrum of unbound states corresponds a linear oscillatory tail [Zabuski, 1968].

The energy of a soliton is proportional to $(\delta n/n_0)^2 D$. For non-planar expanding solitons the energy will decay due to geometry as $1/r$ and $1/r^2$, for cylindrical and spherical geometries, respectively. When combining this geometrical decay with characteristic 4 we find that the soliton amplitude will decay as

$$\frac{\delta n}{n_0} \propto r^{\eta}, \tag{2.60}$$

where r is the radius of the soliton and $\eta = -2/3$ for a cylindrical geometry but $\eta = -4/3$ for a spherical geometry [Hershkowitz et al., 1979; Lonngren,

1983].

Chapter 3

Experimental observations

Since the initial observation of ion-acoustic solitons mentioned in section 1.3 [Ikezi et al., 1970], all experimental efforts have, to our best knowledge, been performed using specially built soliton generation equipment. Most experiments have been performed in some variation of the double-plasma device used by Ikezi et al. In the double-plasma device a background ion density is supplied by an electron gun filament, spraying ionizing electrons into the inert gas. To increase the uniformity of the background plasma, the vacuum chamber is often surrounded by one to two thousand permanent magnets that trap the primary electrons. This enhancement is referred to as the multidipole method [Lonngren, 1983]. In this chapter we report on what we believe to be the first observation of ion-acoustic solitons in a standard plasma processing system: a pulsed magnetron sputtering device. The absence of an initial quiescent background plasma and a very large soliton amplitude differentiates this method significantly from earlier forms of soliton generation.
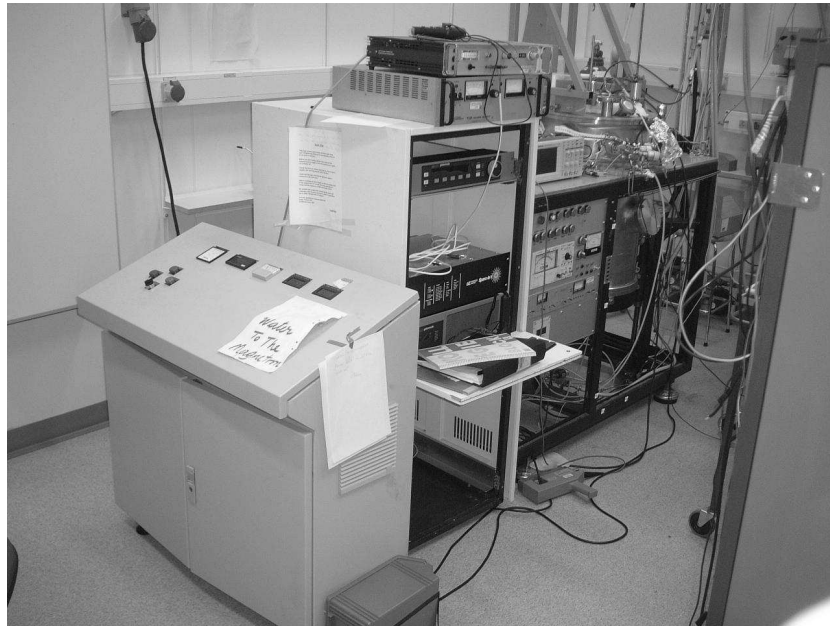
Figure 3.1: The pulsed magnetron system. The power supply is on the left and can provide power up to 2.4 MW during a pulse width of 50 – 100 μs with a repetition frequency of 50 pulses per second. The stainless steel sputtering chamber is on the right.

3.1   Experimental apparatus

The measurements were carried out in a high-power unipolar pulsed magnetron sputtering system at the Department of Physics and Measurement Technology, Lingköping University, Sweden. Figure 3.1 shows a photograph of the system. To the left is a novel type of pulsed power supply, produced by Chemfilt R&D, Sweden, which is used in the experiment. It can deliver peak power pulses of up to 2.4 MW (2000 V and 1200 A) at a repetition frequency of 50 pulses per second (20 ms between pulses) and pulse width in the range of 50 – 100 μs. A pulse width of approximately 70 μs and pulse energies in the range 3 – 6 J were used. To the right in the
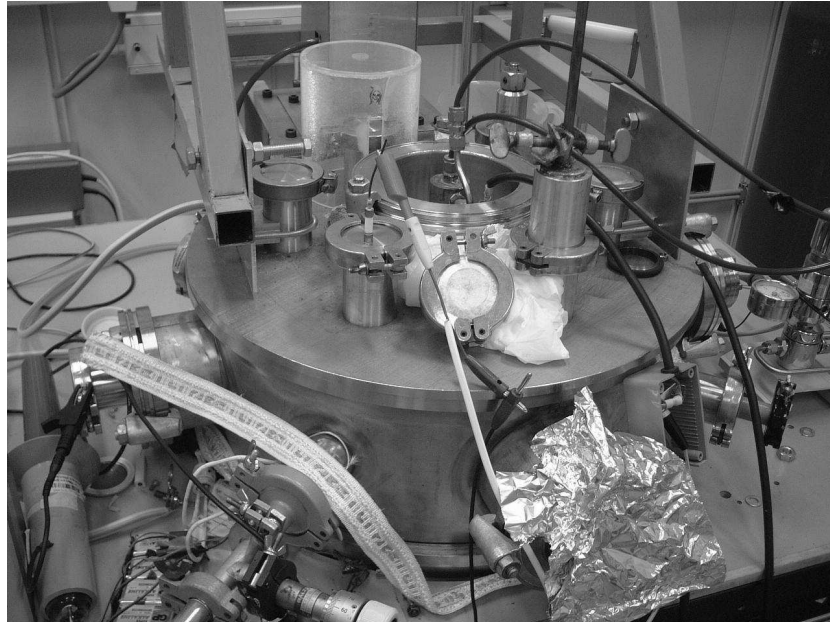
Figure 3.2: Top view of the sputtering chamber. The balanced planar magnetron is mounted on the top lid of a cylindrically symmetric stainless steel sputtering chamber of radius $R = 24$ cm and height $L = 75$ cm. The target has a diameter of 150 mm.
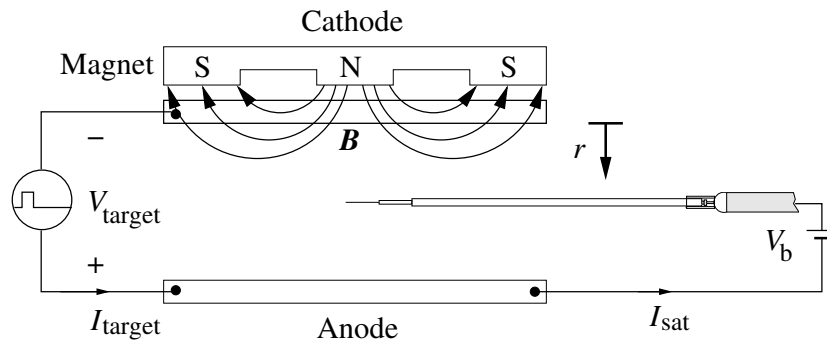
Figure 3.3: A schematic drawing of the experiment. The Langmuir probe was mounted on a movable pole and the tip placed on the axis of the chamber at distances r from the target in the range $4 - 9$ cm. The probe was biased to electron saturation with a constant $V_b = 9$V. The electron saturation current I_{sat} as a function of the time from pulse start t was measured at each probe location.
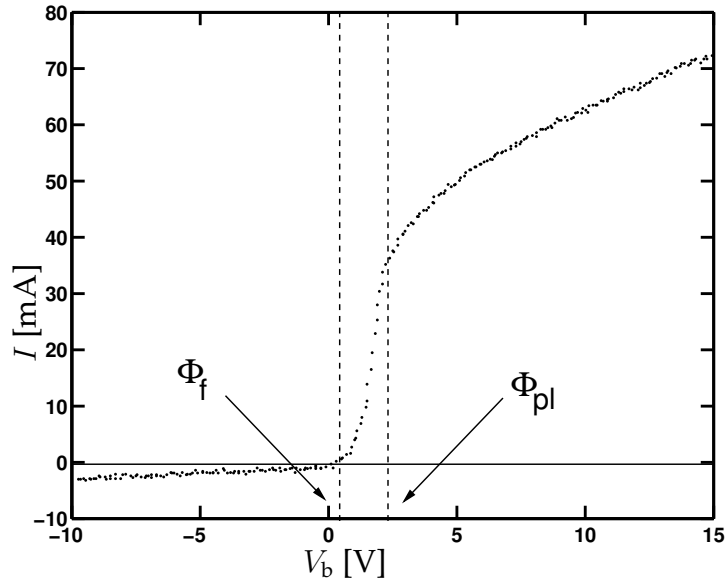
Figure 3.4: Probe current versus probe bias at an arbitrary time instance. The floating potential is $\Phi_f = 0.4$ V and the plasma potential is $\Phi_f = 2.4$ V. The pressure was 5 mTorr and pulse energy 6 J.

figure is the stainless steel sputtering chamber. It has a radius $R = 24$ cm and height $L = 75$ cm. A close up photo of the chamber top lid is shown in figure 3.2. In the center the power cabling and water cooling for the magnetron are visible. It is of the balanced planar type [Waits, 1978; Kelly and Arnell, 2000] and was operated with a titanium target, 150 mm in diameter. Argon of purity 99.9997% and pressure 5 mTorr was used as discharge gas. The base vacuum pressure was approximately 1×10^{-6} Torr.

Electron density perturbations were detected using a cylindrical Langmuir probe made from a tungsten wire of length $l_{pr} = (5.0 \pm 0.5)$ mm and radius $r_{pr} = (50 \pm 1)$ μm. Time curves of the probe current, target current and target voltage were collected with a digital oscilloscope. The probe was placed on the axis of the chamber as shown in figure 3.3 and mea-

surements were performed at distances r from the target in the range $4-9$ cm. As with any other electrode in contact with a plasma, the probe is surrounded by an electron-depleted region known as the *sheath*. The sheath forms because the mobile electrons are more likely to be lost to the probe surface than the heavy ions. A balance is reached by the build up of a potential difference in the sheath region, referred to as the *plasma potential* Φ_{pl}. For each time value the full *I-V* curve of the probe had previously been measured [Alami et al., 2003b] and a representative measurement is shown in figure 3.4. The upper kink in the curve occurs when the applied probe bias reaches the plasma potential. This point is known as *electron saturation*, since above it all current is carried by electrons. The slight increase in probe current above electron saturation is due to an increasing effective collection area.

Zero probe current occurs when electron and ion currents balance. The probe bias at this point equals the potential at which an insulated probe, that can not draw current, would float. It is aptly named *floating potential* Φ_{f}. In the case of a pulsed discharge the plasma and floating potentials are time dependent. The simplest way to estimate the electron density is to ensure that the probe remains at electron saturation at all times. Then the electron density, n_{e}, can be taken to be proportional to the saturation probe current, I_{sat} (ignoring the influence of the changing effective collection area) [Lieberman and Lichtenberg, 1994, p. $174-175$]

$$n_{\text{e}} \propto I_{\text{sat}}. \tag{3.1}$$

In this pursuit a constant probe bias of $V_{\mathrm{b}} = 9$ V was applied to the probe. Although we measure the electron density, our data represents ion-motion as well since the assumption of quasi neutrality, $n_{\mathrm{i}} \approx n_{\mathrm{e}}$, is valid on the time scale considered. In fact the electron density can also be modeled by the same KdV equation as the ions [Washimi and Taniuti, 1966], but traditionally the KdV equation for ions is used. Direct comparison of the temporal behavior of ion and electron densities in the system have shown that electrons and ions behave similarly [Alami et al., 2003a].

3.2   Experimental results

Representative behavior of the probe electron saturation current I_{sat} as a function of time t from the initiation of the target voltage pulse, at distances r of 4, 6, and 8 cm below the target, is shown in figures $3.5 - 3.8$. The pulse energy is 3 J in figure 3.5, 4 J in figure 3.6, 5 J in figure 3.7, and 6 J in figure 3.8. The curves are arbitrarily translated, for clarity, but in each individual figure the curves are drawn to the same scale. All the curves show similar behavior. Before the pulse, no probe current is measured since the plasma from the last pulse has died out completely. Then, a few microseconds after pulse initiation, one or more peaks traveling away from the target reach the probe. Each individual peak, that could clearly be identified, is labeled with a number. In figures 3.5, and 3.8 only one peak was clearly identifiable, two could be identified in figure 3.6 and three in figure 3.7. Examining the curve at 4 cm in figure 3.7 more closely, we notice a strong initial peak (labeled 1) traveling away from the target. In the trailing side

PSfrag replacements

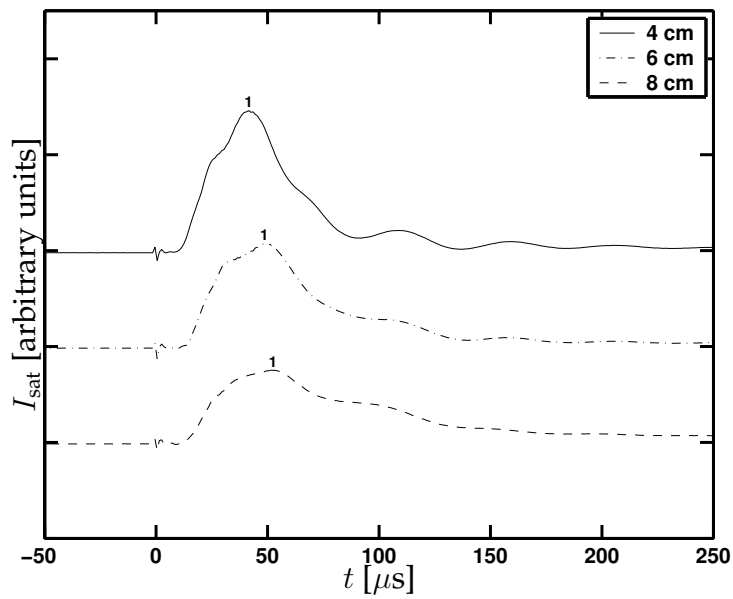Figure 3.5: Electron saturation current, measured by a Langmuir probe, as a function of time from pulse initiation at locations 4, 6, and 8 cm below the target. The curves are arbitrarily translated but drawn to scale. The argon pressure was 5 mTorr, the target made of titanium, pulse length was ≈ 70 μs, and pulse energy 3 J. One individual peak (labeled 1) could clearly be identified.
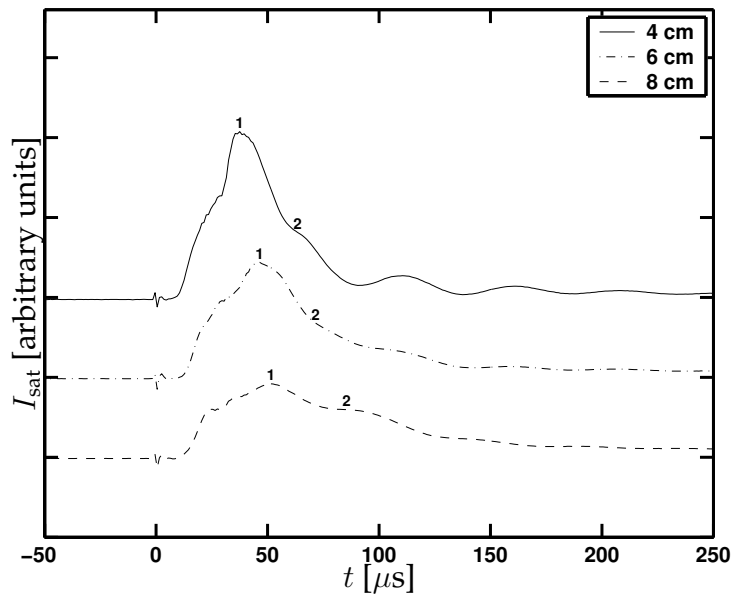
Figure 3.6: Same measurement as in figure 3.5 for a pulse energy of 4 J. Two individual peaks (labeled 1 and 2) could clearly be identified.
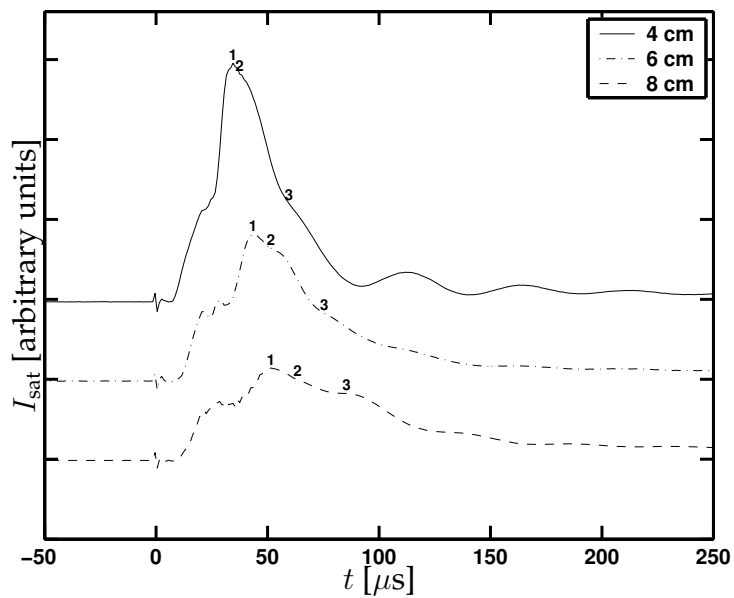

Figure 3.7: Same measurement as in figure 3.5 for a pulse energy of 5 J. Three individual peaks (labeled 1, 2, and 3) could clearly be identified.
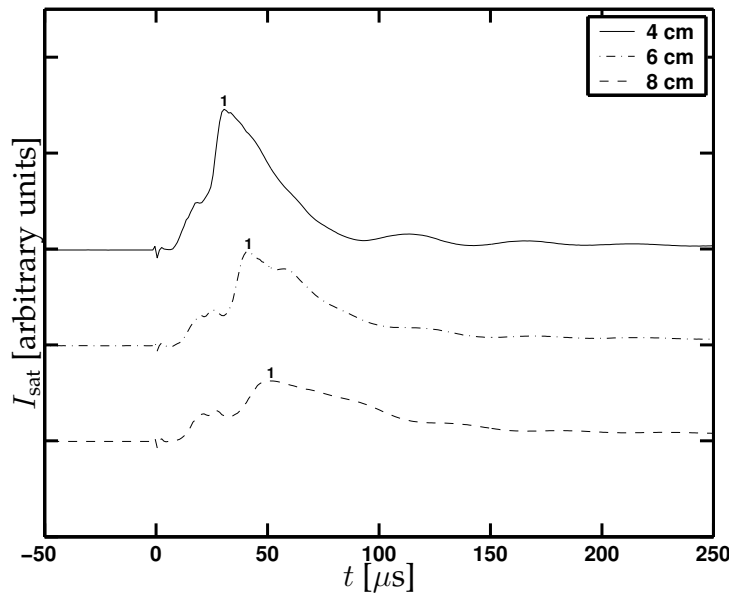
Figure 3.8: Same measurement as in figure 3.5 for a pulse energy of 6 J. One individual peak (labeled 1) could clearly be identified.

of this first peak two other peaks (labeled 2 and 3) can be seen emerging. The three initial peaks are followed by a temporally decaying oscillatory tail of a lesser amplitude. At 6 cm the three peaks have separated further and the second peak has become particularly visible. In all the figures the peaks decay considerably while traveling from 4 to 8 cm, but retain their identity. In contrast the oscillatory tail disperses quite rapidly and at 6 cm it is barely visible. A precursor precedes the first peak at all pulse energies. Taylor et al. [1970] attribute this precursor to a group of streaming ions reflected from the wave front. Similar phenomena were reported by Ikezi et al. [1970]. The dip in probe current at time $t = 0$ is very probably just interference from the target power supply. In general the behavior of the peaks in figures 3.5 – 3.8 conforms with soliton characteristic 1 listed in

section 2.4, regarding an initial compressive density perturbation. Characteristic 2 can not easily be verified since the exact form of the initial density perturbation is unknown.

3.3   Discussion

The waveforms of target voltage V_{target} and target current I_{target} for the measurements of figures 3.5 – 3.8 are shown on the left axis in figures 3.9 – 3.12. The corresponding peak trajectories are shown on the right axis of the figures. The target voltage rises abruptly at $t = 0$ μs but falls as the gas in the chamber breaks down and the target current increases. The voltage seems to reach a plateau close to 400 V at the time of peak target current. The plateau level seems to decrease with higher pulse energy (and peak current).

The first obvious feature of the peak trajectories is that all the peaks travel with a fixed velocity. This velocity was determined using a least squares fit. By extending the fitted line we find that the first peak for each pulse energy is created in the time range of 10 – 30 μs after pulse initiation and that the trend seems to be that at higher pulse energies the peaks emerge sooner in the pulse. A similar trend can be seen in the time of the target current peak. In the figures where more than one peak could be discerned, and traced through the measurements at different distances from the target, (figs. 3.10 and 3.11) two observations can be made. The first one is that the velocity of a peak depends on its amplitude, i.e. larger peaks travel faster than smaller peaks. This is typical for a nonlinear phe-
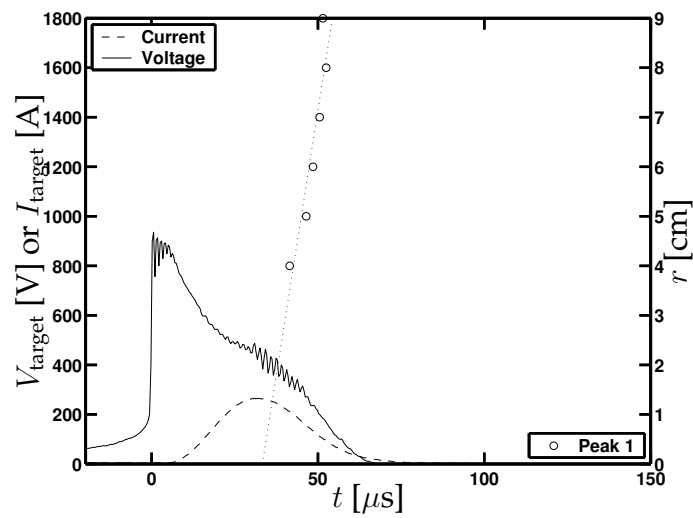
Figure 3.9: The left axis shows the applied target voltage and current. The right axis shows the position of the density peaks. Both are plotted versus the time from pulse initiation. The argon pressure was 5 mTorr, the target made of titanium, and the pulse energy 3 J. The maximum target current occurs at $t = 30$ μs. The density peak travels with a fixed velocity of 4.3×10^3 m/s and is formed roughly 30 μs after pulse initiation.

Figure 3.10: Same plots as in figure 3.9 for pulse energy 4 J. The maximum target current occurs at $t = 30$ μs. Density peak 1 travels with a velocity of 3.2×10^3 m/s and is formed roughly 30 μs after pulse initiation. Peak 2 has a velocity of 1.9×10^3 m/s and is formed roughly 40 μs after pulse initiation.

Figure 3.11: Same plots as in figure 3.9 for pulse energy 5 J. The maximum target current occurs at $t = 28$ μs. Density peaks 1 and 2 travel with velocities of 2.4×10^3 m/s and 1.8×10^3 m/s respectively and are formed roughly 20 μs after pulse initiation. Peak 3 has a velocity of 1.7×10^3 m/s and is formed roughly 40 μs after pulse initiation.
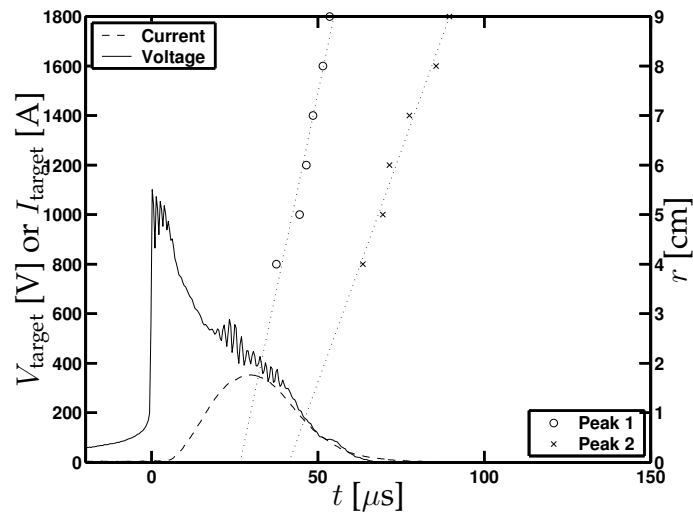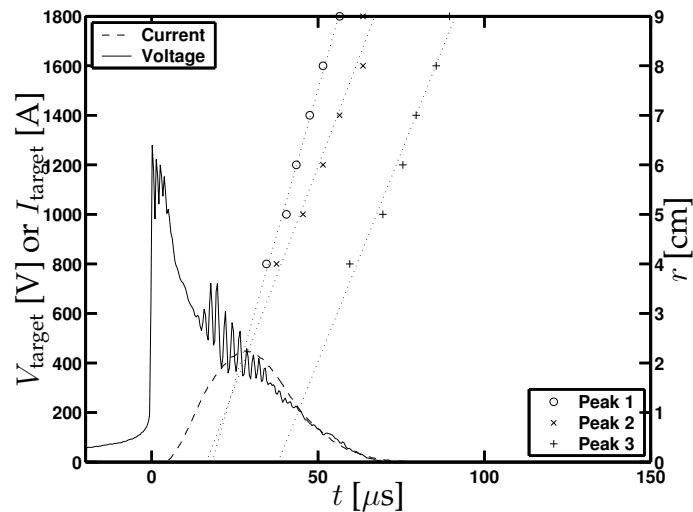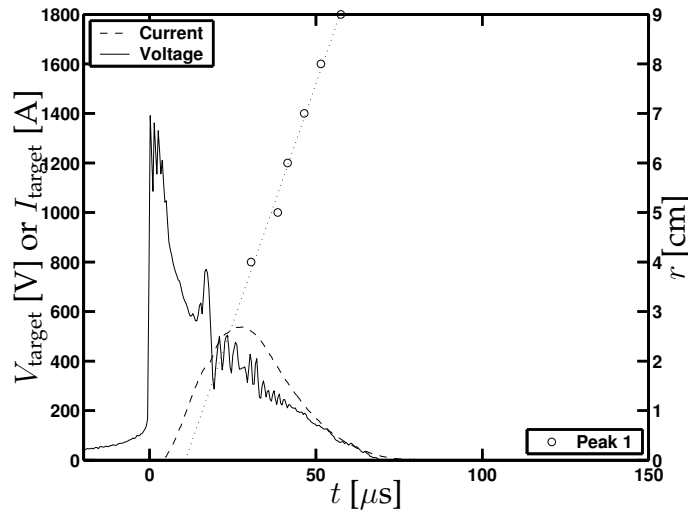
Figure 3.12: Same plots as in figure 3.9 for pulse energy 6 J. The maximum target current occurs at $t = 28$ μs. The density peak travels with a velocity of 1.9×10^3 m/s and is formed roughly 10 μs after pulse initiation.

nomenon. The latter observation is that the second peak can either emerge at the same time as the first one or at a later time. The emergence of more than one peak at the same time can be understood in terms of the n-soliton solution of the KdV equation [Hershkowitz et al., 1972], i.e. multiple superimposed solitons, created from the same initial density perturbation, that spread out because of their relative velocity differences. The emergence of a peak at a later time is harder to explain. One possible explanation is that the peaks created at later times are in fact not due to argon ions but to ionized sputtered metal atoms.

Sputtered metal atoms leave the target surface with relatively high energies, typically on the order of a few eV. These atoms traverse the dense plasma region in a few microseconds. In a conventional dc magnetron discharge the plasma density is too low and the traversing time

too short for appreciable ionization of the metal to occur. In contrast, in the high power pulsed discharge the sputtered atoms can not penetrate the dense plasma without collisions and significant ionization [Ehiasarian et al., 2002]. Thus a high metal ion to neutral fraction is seen in this type of discharge [Helmersson et al., 2000; Bohlmark et al., 2003]. Note that only neutrals are sputtered from the target and all the titanium ions created in the discharge are due to electron impact ionization, which depends strongly on the electron temperature.

If the peaks created at later times are due to a different ion species we can draw the conclusion from equation (2.58) that they should have a different soliton velocity, since the ion-acoustic velocity depends on the ion mass. Furthermore, if both ion species are existent in the plasma at the same time, a modification of the KdV equation has to be made [Tran, 1974]. However our choice of target is not a very suitable one in this regard, since titanium ions have only 20% higher mass than the argon ions, and we do not have enough data to draw any conclusions from this. In what follows we assume only argon ions. For reference, titan has a relative atomic mass of 47.88 and an ionization energy of 6.82 eV. Argon has relative atomic mass of 39.95 and an ionization energy of 15.8 eV, significantly higher than that of titan.

Optical emission spectroscopy measurements of the system, with a chromium target in an argon discharge at 3 mTorr, showed three distinct stages. During the first 10 μs the emission is dominated by argon atom lines when the breakdown occurs. Then, as Ar is ionized the plasma density and target current increase and Ar^+ emission is detected. A few mi-

croseconds later Cr^+ ions are detected and at approximately 30 μs after the initiation of the pulse the Cr^+ emission peaks [Ehiasarian et al., 2002]. Chromium has a relative atomic mass close to argon (52.00) and a ionization energy close to titan (6.77 eV). A similar measurement of Ar and Ti neutral lines also shows a time separation [Macák et al., 2000]. These results support the idea that the pulses created at later times might be due to ionized metal but simultaneous optical and probe measurements would be necessary to confirm this.

To get a more quantitative comparison of the observed soliton characteristics with theory, we start by plotting the maximum density perturbation $\delta n / n_0$ of the first peak measured at various distances r from the magnetron target on a log-log scale in figure 3.13. Since our system lacks an initial background plasma we take n_0 to be proportional to the seemingly stable probe current remaining after the solitons have past. This value increases noticeably with increasing r, since the density addition from the dispersing tail has a relatively large impact on the low background density level. To avoid the trend introduced by this effect an average of n_0 over all r was used.

Intuitively one would expect a spherical symmetry of expanding waves in our system since the diameter of the target (15 cm) is much smaller than that of the chamber (48 cm). Waves originating at the target can thus expand unrestricted into the half-sphere below. In fact observations of spherical solitons, excited by a small circular plate, have been reported [Hershkowitz et al., 1979]. The solid line in figure 3.13 has a slope of $-4/3$ and represents the prediction of equation (2.60) for a spherical soliton. At
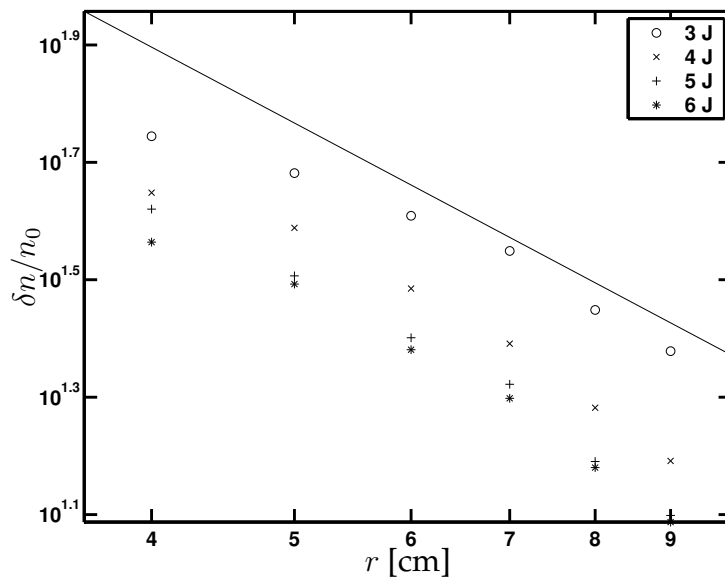
Figure 3.13: The maximum density perturbation $\delta n/n_0$ of the leading peak measured at various distances r from the magnetron target for pulse energies of $3-6$ J. The process gas was argon at 5 mTorr and the target was made of titanium. The solid line has a slope of $-4/3$.
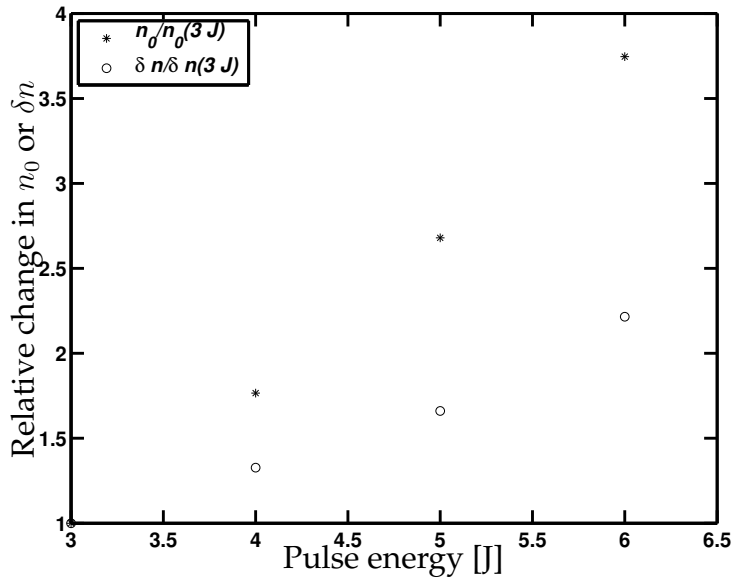
Figure 3.14: The relative changes in average background density $n_0/n_0(3\,\text{J})$ and in amplitude of the leading peak $\delta n/\delta n(3\,\text{J})$ at 6 cm below the target, versus pulse power.

distances greater than 5 cm below the target, the peaks follow the polynomial decay model closely. Nearest to the target the decay is slower and may be due to the fact that ionization is still active (the target current is still sizable as seen in figures 3.9 – 3.12). At distances greater than 7 cm the balance between nonlinearity and dispersion seems to tip in favor of the latter and the decay increases as dispersion takes over. Similar behavior has been observed for spherical solitons by Ze et al. [1979a].

It is interesting to note that in figure 3.13 the peaks at a pulse power of 3 J (the lowest value) have the largest density perturbation $\delta n/n_0$. This is due to the fact that although both the absolute value of the peak density n_{peak}, and the value of $\delta n = n_{\text{peak}} - n_0$, grow with increasing power, the background density n_0 grows even faster. The net result is that the ratio
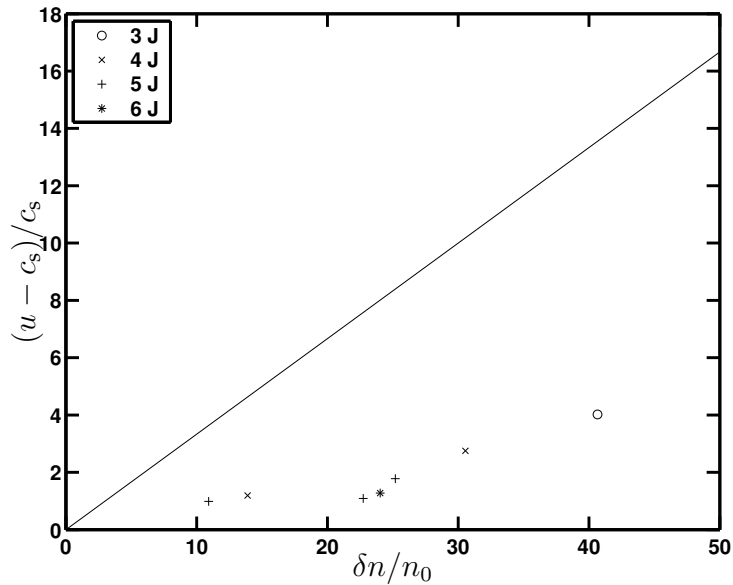
Figure 3.15: The velocity of the soliton peaks, shifted and normalized by the ion-acoustic velocity, versus their maximum density perturbation at 6 cm below the target for pulse energies of $3 - 6$ J. The process gas was argon at 5 mTorr and the target made of titanium. The solid line shows the relation $(u - c_\mathrm{s})/c_\mathrm{s} = 1/3 \delta n/n_0$.

$\delta n/n_0$ actually decreases with increasing power. This effect is presented in figure 3.14, which shows the relative changes in n_0, and δn at 6 cm below the target, with increasing pulse power. Optical emission spectroscopy measurements of the system have also showed increased ionization with increased peak target current for a chromium target in an argon discharge at 3 mTorr [Ehiasarian et al., 2002].

Next we examine the soliton velocity relation of characteristic 3. We plot the velocity of the soliton peaks, shifted and normalized by the ion acoustic velocity, versus the maximum density perturbation of each peak, at 6 cm below the target, for different pulse energies in figure 3.15. The later peaks are included in the figure for the energy values at which mul-

tiple peaks could be measured. The solid line shows the prediction of equation (2.58. Since in our system we do not have an auxiliary supply of background plasma, we can not simply measure the ion-acoustic velocity by exciting a small amplitude wave. Thus to get a value for c_s we need an estimate of the electron temperature. The time evolution of the electron energy probability function in the same experimental setup, using a tantalum target, has been studied by Gudmundsson et al. [2002]. In light of those results we estimate an electron temperature of $T_e = 0.3$ eV at 5 mTorr, for the colder bulk plasma remaining after the solitons have past. The value of n_0 is found by averaging over all r as before. The figure clearly demonstrates that the peaks with largest density perturbation have the highest velocity. The observed relation is linear but the constant of proportionality is close to $\alpha = 0.1$, slightly lower than the $\alpha = 1/3$ to be expected for a one dimensional soliton. It should be noted that the uncertainty in the electron temperature affects only the slope of the line but does not change the fact that the observed relation is linear. We suggest that the discrepancy in the velocity relation could be due to the fact that the density perturbation observed is two orders of magnitude higher than what previously has been reported [Ikezi et al., 1970; Hershkowitz et al., 1979; Lee et al., 1996] and since Washimi and Taniuti [1966] assume a small perturbation in their derivation the simple model presented in section 2.4 may not fully apply. Previous experiments on cylindrical and spherical solitons have also shown even greater departure from the model. A value of $\alpha = 1$ was reported for expanding cylindrical solitons [Hershkowitz and Romesser, 1974] and values of 1.5 [Hershkowitz et al., 1979], 0.4 [Ze
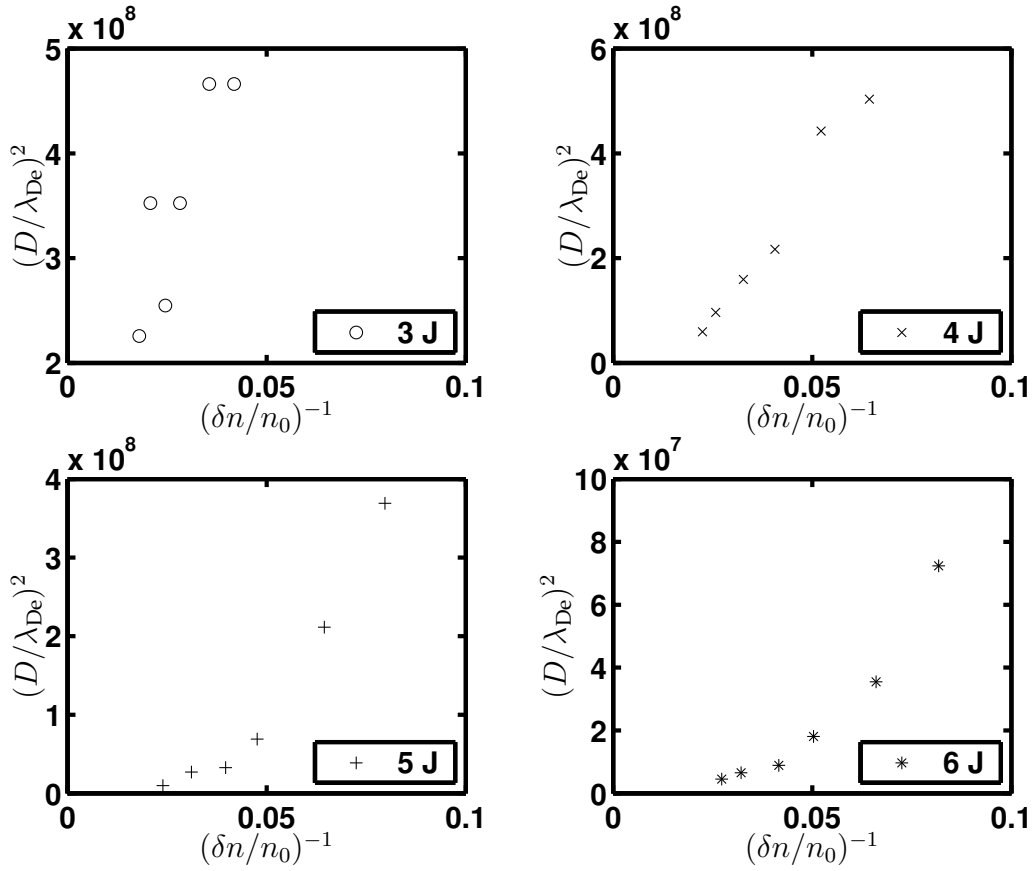
Figure 3.16: The square of the normalized spatial width of the soliton peaks versus the inverse maximum density perturbation for pulse energies of $3 - 6$ J. The process gas was argon at 5 mTorr and the target made of titanium.

et al., 1979a], and 0.3 [Ze et al., 1979b] have been reported for expanding spherical solitons.

Finally we examine characteristic 4, the relation between soliton spatial width D and the maximum density perturbation $\delta n/n_0$. The width was measured as follows. First the full width at the half maximum was measured from the temporal signal shown in figures 3.5 – 3.8. Next the spatial width was obtained by multiplying the temporal width with the

velocity of the soliton [Nakamura and Sugai, 1996]. We plot $(D/\lambda_{\mathrm{De}})^2$ versus $(\delta n/n_0)^{-1}$ in figure 3.16. The width is scaled by the electron Debye length λ_{De}. Each sub-plot gives a trace from 4 to 9 cm below the target for one pulse energy. The absolute value of the electron density after the solitons have past is estimated 2×10^{17} m^{-3} at 5 mTorr [Gudmundsson et al., 2002]. This value is only needed to estimate the electron Debye length and corresponds to a value of $\lambda_{\mathrm{De}} = 9$ μm. For n_0 we use an average over all r. According to theory, $(D/\lambda_{\mathrm{De}})^2$ should depend linearly on $(\delta n/n)^{-1}$. The figures clearly indicates this property for each pulse energy. We can also clearly see the effect that the deviation from the decay property, shown in figure 3.13, has on the relation. At low $(\delta n/n_0)^{-1}$ (high $\delta n/n_0$ and and close to the target) the peaks show the linear predicted relationship. For higher values of $(\delta n/n_0)$ (far from the target) the dispersion takes over and the width of the peaks increases beyond what to be expected. The collision property (characteristic 5) can not be tested with this configuration since only one source of solitons is present.

In summary, we observe a positive density perturbation that evolves into multiple solitons that travel with a fixed velocity away from the magnetron target. The rate of decay of the soliton amplitude indicates spherical symmetry. Although the density perturbation is higher than previously reported, the simple model presented predicts the observed behavior quite well. The soliton velocities depend linearly on amplitude and the square of the spatial width is proportional to the inverse amplitude.

Chapter 4

Conclusions

An overview of sputtering devices was given, with emphasis on the magnetron sputtering method. We introduced a refinement of the magnetron method, known as unipolar pulsed magnetron sputtering, and elaborated on its superiority to conventional dc magnetron sputtering devices regarding target utilization and ionization of sputtered particles. A short overview of recent experimental work on the system was given.

The properties of waves in nonlinear and dispersive systems were reviewed and the fluid model of a plasma was introduced. We derived the Korteweg-de Vries equation describing planar ion-acoustic waves of finite amplitude and examined the characteristics of one-dimensional ion-acoustic solitons in a plasma.

Experimental evidence for the existence of ion-acoustic solitons in a unipolar pulsed magnetron discharge was given and thus a new method for generating ion-acoustic solitons of high amplitude, without the presence of a quiescent background plasma has been presented. We confirmed

that the solitons generated fulfill the basic properties of the soliton solution of the Korteweg-de Vries equation in a spherical geometry.

Our measurements suggest that soliton peaks emerge at two different times after the initiation of the magnetron target pulse. Comparison with optical emission spectroscopy data lead to speculation of weather the peaks created at later times might consist mainly of ionized sputtered metal atoms. If true this could pave the way for interesting temporal control of the ion flux to the substrate during coating. Further optical emission measurements combined with probe measurements are necessary to resolve this issue.

Acknowledgement

knowledged for the use of the power supply.

Bibliography

J. Alami, J. T. Gudmundsson, J. Böhlmark, K. B. Gylfason, and U. Helmersson. Plasma parameters during high power pulsed magnetron sputtering. To be published in the Proceedings of the 16th International Symposium on Plasma Chemistry (ISPC-16), (Taormina, Italy, 2003)., 2003a.

J. Alami, J. T. Gudmundsson, J. Böhlmark, and U. Helmersson. Dynamics of the plasma parameters in a unipolar high power pulsed magnetron discharge (power influence). To be published in Surface & Coatings Technology, 2003b.

J. Bohlmark, J. Alami, J. T. Gudmundsson, and U. Helmersson. Ionization of sputtered Ti during high power pulsed magnetron sputtering. To be published in the Proceedings of the seventh International Symposium on Sputtering and Plasma Processes (ISSP-2003), (Kanazawa, Japan, June 11th - 13th 2003)., 2003.

John S. Chapin. The planar magnetron. *Research/Development*, 25(1):37 – 40, January 1974.

Francis F. Chen. *Introduction to Plasma Physics and Controlled Fusion*, volume 1. Plenum Press, New York, U.S.A., second edition, 1984. ISBN 0-306-41332-9.

Richard O. Dendy, editor. *Plasma Physics: An Introductory Course*. Cambridge University Press, Cambridge, U.K., 1993. ISBN 0-521-43309-6. Collection of lectures given at the Culham Summer School in Plasma Physics.

R. K. Dodd, J. C. Eilbeck, J. D. Gibbons, and H. C. Morris. *Solitons and Nonlinear Wave Equations*. Academic Press, London, U.K., 1982. ISBN 0-12-219122-6.

A. P. Ehiasarian, R. New, W.-D. Münz, L. Hultman, U. Helmersson, and V. Kouznetsov. Influence of high power densities on the composition of pulsed magnetron plasmas. *Vacuum: Surface Engineering, Surface Instrumentation & Vacuum Technology*, 65:147 – 154, 2002.

J. A. Elliot. *Plasma kinetic theory*, chapter 2, pages 29 – 53. In , Dendy [1993], 1993. ISBN 0-521-43309-6. Collection of lectures given at the Culham Summer School in Plasma Physics.

Enrico Fermi, John R. Pasta, and Stanislaw M. Ulam. Studies of nonlinear problems. I. Technical Report LA-1940, Los Alamos Scientific Laboratory, May 1955.

Clifford S. Gardner, John M. Greene, Martin D. Kruskal, and Robert M. Miura. Method for solving the Korteweg-deVries equation. *Physical Review Letters*, 19:1095 – 1097, 1967.

J. T. Gudmundsson, J. Alami, and U. Helmersson. Evolution of the electron energy distribution and plasma parameters in a pulsed magnetron discharge. *Applied Physics Letters*, 78:3427 – 3429, 2001.

J. T. Gudmundsson, J. Alami, and U. Helmersson. Spatial and temporal behavior of the plasma parameters in a pulsed magnetron discharge. *Surface & Coatings Technology*, 161:249 – 256, 2002.

U. Helmersson, Z. S. Kahn, and J. Alami. Ionized-PVD by pulsed sputtering of Ta for metallization og high-aspect-ratio structures in VLSI. In *The Third International Euroconference on Advanced Semiconductor Devices and Microsystems*, pages 191 – 193, Somolenice Castle Slovakia, october 2000.

Noah Hershkowitz, J. Glanz, and Karl E. Lonngren. Spherical ion-acoustic solitons. *Plasma Physics*, 21:583 – 588, 1979.

Noah Hershkowitz and Thomas Romesser. Observations of ion-acoustic cylindrical solitons. *Physical Review Letters*, 32:581 – 583, 1974.

Noah Hershkowitz, Thomas Romesser, and David Montgomery. Multiple soliton production and the Korteweg-de Vries equation. *Physical Review Letters*, 29:1586 – 1589, 1972.

H. Ikezi. Experiments on ion-acoustic solitary waves. *Physics of Fluids*, 16: 1668 – 1675, 1973.

H. Ikezi, R. J. Taylor, and D. R. Baker. Formation and interactions of ion-acoustic solitons. *Physical Review Letters*, 25:11 – 14, 1970.

S. Kadlec, J. Musil, and W.-D. Münz. Sputtering systems with magnetically enhanced ionization for ion plating of TiN films. *Journal of Vacuum Science and Technology A*, 8:1318–1324, 1990.

P. J. Kelly and R. D. Arnell. Magnetron sputtering: a review of recent developments an applications. *Vacuum: Surface Engineering, Surface Instrumentation & Vacuum Technology*, 56:159 – 172, 2000.

P. J. Kelly, P. S. Henderson, R. D. Arnell, G. A. Roche, and D. Carter. Reactive pulsed magnetron sputtering process for alumina films. *Journal of Vacuum Science and Technology A*, 18:2890–2896, 2000.

Vladimir Kouznetsov, Karol Macák, Jochen M. Schneider, Ulf Helmersson, and Ivan Petrov. A novel pulsed magnetron sputter technique utilizing very high target power densities. *Surface & Coatings Technology*, 122:290 – 293, 1999.

S.-G. Lee, D. A. Diebold, N. Hershkowitz, and P. Moroz. Wide solitons in an ion-beam-plasma system. *Physical Review Letters*, 77:1290 – 1293, 1996.

Michael A. Lieberman and Allan J. Lichtenberg. *Principles of Plasma Discharges and Materials Processing*. John Wiley & Sons, Inc., New York, U.S.A., 1994. ISBN 0-471-00577-0.

Karl E. Lonngren. Soliton experiments in plasmas. *Plasma Physics*, 25:943 – 982, 1983.

Karol Macák, Vladimir Kouznetsov, Jochen Schneider, Ulf Helmersson, and Ivan Petrov. Ionized sputter deposition using an extremely high plasma density pulsed magnetron discharge. *Journal of Vacuum Science and Technology A*, 18:1533 – 1537, 2000.

Stephen Maxon and James Viecelli. Cylindrical solitons. *Physics of Fluids*, 17:1614 – 1616, 1974a.

Stephen Maxon and James Viecelli. Spherical solitons. *Physical Review Letters*, 32:4 – 6, 1974b.

Y. Nakamura, H. Bailung, and P. K. Shukla. Observation of ion-acoustic shocks in a dusty plasma. *Physical Review Letters*, 83:1602 – 1605, 1999.

Y. Nakamura and H. Sugai. Experiments on ion-acoustic solitons in a plasma. *Chaos, Solitons & Fractals*, 7:1023 – 1031, 1996.

Dwight Roy Nicholson. *Introduction to Plasma Theory*. John Wiley & Sons, Inc, New York, U.S.A., 1983. ISBN 0-471-09045-X.

Joseph Proud, editor. *Plasma Processing of Materials, Scientific Opportunities and Technological Challenges*. National Academy Press, Washington, D.C., 1991.

Michel Remoissenet. *Waves Called Solitons: Concepts and Experiments*. Springer-Verlag, Berlin, Germany, 1996. ISBN 7-5062-4105-6.

S. M. Rossnagel and J. Hopwood. Magnetron sputter deposition with high levels of metal ionization. *Applied Physics Letters*, 63:3285 – 3287, 1993.

S. M. Rossnagel and J. Hopwood. Metal ion deposition from ionized mangetron sputtering discharge. *Journal of Vacuum Science and Technology B*, 12:449 – 453, 1994.

S. Schiller, K. Goedicke, J. Reschke, V. Kirchhoff, S. Schneider, and F. Milde. Pulsed magnetron sputter technology. *Surface & Coatings Technology*, 61: 331 – 337, 1993.

Donald Leonard Smith. *Thin-Film Deposition: Principles and Practice*. McGraw-Hill, Inc., New York, U.S.A., 1995. ISBN 0-07-058502-4.

Takami Takeuchi, Satoru Iizuka, and Noriyoshi Sato. Ion acoustic shocks formed in a collisionless plasma with negative ions. *Physical Review Letters*, 80:77 – 80, 1998.

R. J. Taylor, D. R. Baker, and H. Ikezi. Observation of collisionless electrostatic shocks. *Physical Review Letters*, 24:206 – 209, 1970.

John A. Thornton. The microstructure of sputter-deposited coatings. *Journal of Vacuum Science and Technology A*, 4:3059 – 3065, 1986.

M. Q. Tran. Propagation of solitary waves in a two ion species plasma with finite ion temperature. *Plasma Physics*, 16:1167 – 1175, 1974.

Robert K. Waits. Planar magnetron sputtering. *Journal of Vacuum Science and Technology*, 15:179 – 187, 1978.

Haruichi Washimi and Tosiya Taniuti. Propagation of ion-acoustic solitary waves of small amplitude. *Physical Review Letters*, 17:996 – 998, 1966.

Helin Wei, Zuli Liu, and Kailun Yao. The influence of the incidence energy of deposited particles on the growth morphology of thin films. *Vacuum: Surface Engineering, Surface Instrumentation & Vacuum Technology*, 57:87 – 97, 2000.

B. Window and N. Savvides. Charged particle fluxes from planar magnetron sputtering sources. *Journal of Vacuum Science and Technology A*, 4: 196–202, 1986a.

B. Window and N. Savvides. Unbalanced dc magnetrons as spources of high ion fluxes. *Journal of Vacuum Science and Technology A*, 4:453–456, 1986b.

Akira Yonesu, Takashi Kato, Hiroki Takemoto, Naoki Nishimura, and Yasumasa Yamashiror. Cylindrical DC magnetron sputtering assisted by microwave plasma. *Japanese Journal of Applied Physics*, 38:4326 – 4328, 1999.

N. J. Zabuski and M. D. Kruskal. Interaction of "solitons" in a collisionless plasma and the recurrence of initial states. *Physical Review Letters*, 15:240 – 243, 1965.

Norman. J. Zabuski. Solitons and bound states of the time-independent schrödinger equation. *Physical Review*, 168:124 – 168, 1968.

Frederic Ze, Noah Hershkowitz, Chung Chan, and Karl E. Lonngren. Exitation of spherical ion acoustic solitons with a conducting probe. *Physics of Fluids*, 22:1554 – 1557, 1979a.

Frederic Ze, Noah Hershkowitz, Chung Chan, and Karl E. Lonngren. Inelastic collision of spherical ion-acoustic solitons. *Physical Review Letters*, 42:1747 – 1750, 1979b.